

Intrinsic resistance to RAS inhibitors is driven by dysregulation of KRAS degradation

Received: 12 November 2024

Accepted: 13 November 2025

Published online: 15 December 2025

Tonci Ivanisevic^{1,8}, Yan Ma^{1,8}, Emiel Van Boxel^{1,2}, Wout Magits¹,
Benoit Lechat¹, Zeynep Koçberber^{3,4}, Philipp Willnow¹^{3,4},
Sarah-Maria Fendt¹^{3,4}, Greetje Vande Velde¹^{5,6}, Raj Sewduth¹✉ &
Anna A Sablina^{1,7}✉

 Check for updates

Activating mutations in *KRAS* occur in approximately 30% of lung adenocarcinomas. Despite advances in RAS-targeted therapies, intrinsic resistance limits their long-term efficacy. Here, we identify elevated levels of wild-type KRAS (WT-KRAS) protein as a key driver of intrinsic resistance in KRAS-mutant lung tumors. KRAS accumulation results from impaired LZTR1-mediated degradation, triggered either by LZTR1 loss or pharmacological RAS inhibition. Stabilized WT-KRAS activates the mTOR/HIF1α pathway by promoting lysosomal recruitment of the SLC3A2/SLC7A5 amino acid transporter complex, reprogramming lysosomal amino acid sensing. Shallow deletions of *LZTR1*, present in up to 40% of KRAS-mutant lung adenocarcinomas, are associated with increased mTOR activity and may contribute to therapeutic resistance to RAS inhibitors. Co-inhibition of mTOR or the SLC3A2/SLC7A5 complex using dactolisib or JPH203 restores sensitivity to KRAS inhibitors *in vitro* and *in vivo*. These findings support combinatorial targeting of mTOR signaling or amino acid transport to overcome intrinsic resistance in KRAS-mutant lung cancer.

Lung cancer is one of the most common cancers worldwide, with an aggressive clinical course and high mortality rates due to the lack of efficient long-term therapy. Almost 30% of non-small cell lung cancers (NSCLCs) are caused by activating Kirsten rat sarcoma viral oncogene homolog (*KRAS*) mutations¹. Mutations in the *KRAS* gene occur most frequently at codons G12, G13, and Q61 and activate KRAS signaling by either impairing the intrinsic GTPase activity of KRAS or structurally altering KRAS, which makes it insensitive to GTPase-activating proteins².

Targeting RAS has been a central focus during the past four decades, and the efforts have intensified over the past years, stirred by

the discovery of compounds tethered to the cysteine of KRAS^{G12C}. The KRAS^{G12C} mutant-selective inhibitor, sotorasib, is the first FDA-approved targeted therapy against KRAS, in *KRAS*^{G12C}-mutated non-small cell lung cancer (NSCLC). A second KRAS^{G12C} inhibitor, adagrasib, received FDA approval in 2023, and several additional RAS inhibitors have now entered clinical investigation³. Mirati Therapeutics (acquired by Bristol Myers Squibb) and Boehringer Ingelheim have also reported KRAS^{G12D} mutant-selective inhibitors, MRTX1133 and BI-KRAS-G12D^{3,4}. MRTX1133 has demonstrated potent *in vitro* and *in vivo* antitumor efficacy against KRAS-G12D-mutant cancer cells⁵. In addition, AZD0022 is currently being evaluated by AstraZeneca in a Phase I/

¹VIB-KU Leuven Center for Cancer Biology, Leuven, Belgium. ²Biocrystallography, Department of Pharmaceutical and Pharmacological Sciences, KU Leuven, Leuven, Belgium. ³Laboratory of Cellular Metabolism and Metabolic Regulation, VIB Center for Cancer Biology, VIB, Leuven, Belgium. ⁴Laboratory of Cellular Metabolism and Metabolic Regulation, Department of Oncology, KU Leuven and Leuven Cancer Institute (LKI), Leuven, Belgium. ⁵Nuclear Medicine and Molecular Imaging, Department of Imaging and Pathology, KU Leuven, Leuven, Belgium. ⁶Biomedical MRI/MoSAIC, Department of Imaging and Pathology, KU Leuven, Leuven, Belgium. ⁷Department of Oncology, KU Leuven, Leuven, Belgium. ⁸These authors contributed equally: Tonci Ivanisevic, Yan Ma.

✉ e-mail: raj.sewduth@kuleuven.be; anna.sablina@kuleuven.be

IIa trial as a KRASG12D mutant-selective inhibitor in combination with other anti-cancer agents (NCT06599502). Complementing this effort, LY3962673 and INCB161734 from Lilly and Incyte, respectively, demonstrate high potency, oral bioavailability, and robust selectivity for targeting mutant KRAS-G12D (NCT06586515, NCT06179160, respectively).

Sotorasib has demonstrated an overall response rate of approximately 37% in patients with non-small cell lung cancer (NSCLC). However, intrinsic resistance still presents a challenge, as nearly half of the patients experienced stable disease, and all treated patients developed drug resistance during the monitoring phase. This underscores the necessity for further research on resistance mechanisms⁶. While Boehringer Ingelheim has reported the discovery of direct pan-KRAS inhibitors⁷, long-term RAS suppression could also be accomplished by simultaneously targeting several RAS family members. Revolution Medicines has developed cyclophilin A-dependent molecular glues, such as RMC6236 or RMC7977, orally available pan-RAS inhibitors^{8,9}. These Pan-RAS inhibitors presented significant antitumor activity^{9–11}, and recent data from phase I trials evaluating RMC6236 indicated tolerability toward the treatment¹² (NCT05379985). Preliminary clinical activity of pan-RAS inhibition was demonstrated by the fact that nearly one-third of PDAC and NSCLC patients showed a partial response to the treatment¹⁰. Investigating the mechanisms behind intrinsic and acquired resistance to RAS inhibitors is essential for identifying biomarkers that predict treatment response and developing strategies to overcome resistance and improve patient outcomes.

Although numerous studies have examined the role of wild-type (WT) and mutant KRAS allele dosage in tumorigenesis and therapeutic response¹³, they have overlooked the effect of this allele dosage on KRAS protein expression¹⁴. On the other hand, emerging data show that adaptive resistance to KRAS-G12C inhibitors in lung adenocarcinoma is associated with an increase in KRAS protein levels. In addition, genome-wide CRISPR screens have revealed that loss of leucine zipper-like translational regulator 1 (LZTR1), a key regulator of RAS proteostasis, suppresses the response to the KRAS-G12C inhibitor sotorasib¹⁵. The LZTR1/Cullin 3 complex mediates the ubiquitination of the RAS family members, such as KRAS, HRAS, NRAS, MRAS, and RIT1, and regulates their activity through either degradative or non-degradative mechanisms^{16,17}. In addition, to sotorasib, loss of LZTR1 is associated with resistance to tyrosine kinase inhibitors^{18–20} and allosteric inhibitors of SHP2²¹. While these findings suggest that KRAS protein dosage is involved in resistance to anti-RAS therapies, the effects of increased KRAS protein levels and the underlying mechanisms affecting RAS inhibitor response remain unexplored.

Here, we show that the elevated wild-type KRAS (WT-KRAS) protein levels drive intrinsic resistance in KRAS-mutant lung tumors. This accumulation results from impaired degradation by LZTR1, due to either LZTR1 loss or RAS inhibition. Stabilized WT-KRAS activates mTOR/HIF1α signaling by recruiting the SLC3A2/SLC7A5 amino acid transporter to lysosomes, altering nutrient sensing. LZTR1 deletion, found in up to 40% of KRAS-mutant lung cancers, correlate with increased mTOR activity and resistance to RAS inhibitors. Dual targeting of mTOR or the transporter complex with dactolisib or JPH203 restores drug sensitivity, highlighting a strategy to overcome resistance.

Results

RAS inhibitors block LZTR1-mediated degradation of RAS proteins

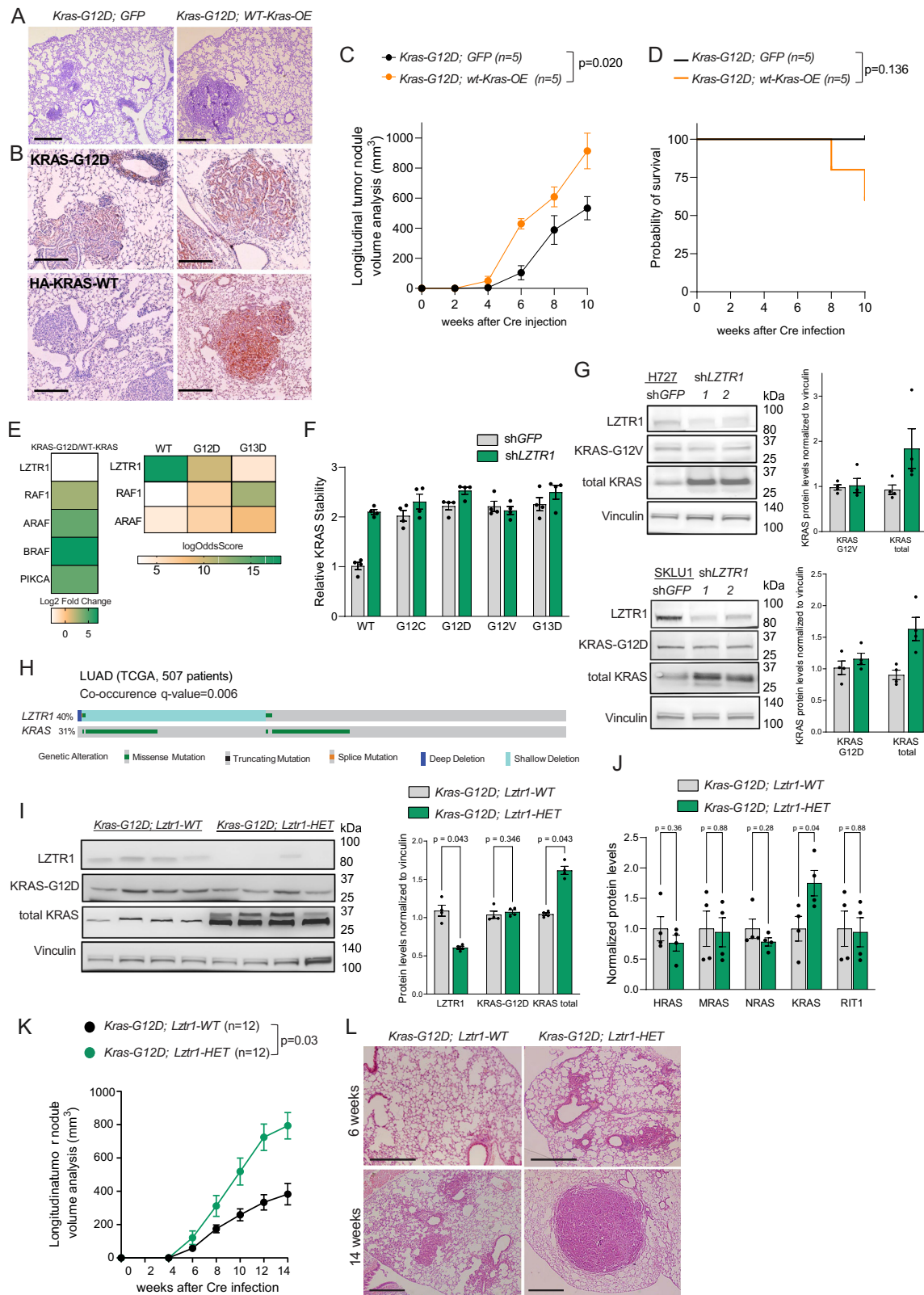
To investigate the impact of KRAS protein dosage beyond traditional allele modulation techniques, we employed two distinct strategies to increase KRAS protein expression *in vivo*, using the *KrasG12D*^{lsl/lsl} mouse model of lung adenocarcinoma induced by an intratracheal administration of a Cre-recombinase expressing virus under the

control of the alveolar type II cell-specific surfactant protein C (*Sftpc*) promoter. As a first approach, we injected a lentivirus encoding Cre-recombinase together with GFP or HA-tagged wild-type (WT-KRAS), driven by the *Sftpc*-specific promoter, in *KrasG12D*^{lsl/lsl} mice. Histological analysis validated the expression of KRAS-G12D upon Cre infection in both *Kras-G12D; GFP* and *Kras-G12D; WT-KRAS-OE* mice (Fig. 1A, B). We also confirmed HA-tagged KRAS overexpression within the tumor nodules of *Kras-G12D; WT-KRAS-OE* mice, which developed large adenoma nodules compared to *Kras-G12D; GFP* mice (Fig. 1A, B). Concordantly, longitudinal micro-computed tomography (micro-CT) volumetric analysis revealed that increased KRAS expression led to accelerated tumor progression and was associated with decreased overall survival, with 30% mortality observed by the tenth week post-injection (Fig. 1C, D).

As a second approach to modulate WT-KRAS protein levels, we employed a *Lztr1* knockout model. Previous studies showed that LZTR1 is more prone to interact with GDP-bound RAS proteins^{22,23} (Fig. 1E), strongly suggesting that LZTR1 is primarily involved in the degradation of KRAS-WT. Consistently, KRAS-WT co-immunoprecipitated with LZTR1 and exhibited increased ubiquitination in LZTR1-overexpressing cells, whereas the KRAS-G12D mutant failed to co-immunoprecipitate with LZTR1 (Supplementary Fig. S1A, B). Moreover, a global protein stability (GPS) analysis using a dual-fluorophore reporter designed to monitor KRAS protein stability revealed that LZTR1 has a markedly stronger effect on the stability of WT-KRAS than on mutant KRAS (Fig. 1F). Immunoblotting with total KRAS and KRAS-G12D-specific antibodies also demonstrated that LZTR1 suppression in lung cancer cell lines increased total KRAS protein levels, without affecting KRAS-G12D abundance, suggesting that the upregulation was restricted to the wild-type protein (Fig. 1G and Supplementary Fig. S1C).

Heterozygous loss of the *LZTR1* locus occurs in approximately 40% of KRAS-mutant lung adenocarcinoma (LUAD) cases in the Cancer Genome Atlas (TCGA) dataset (Fig. 1H) and was associated with decreased *LZTR1* expression and poorer progression-free survival (Supplementary Fig. S1D). Thus, *Lztr1*^{fl/fl}, *Kras*^{G12D}^{lsl/lsl} (*Kras-G12D; Lztr1-HET*) and *Lztr1*^{fl/fl}, *Kras*^{G12D}^{lsl/lsl} (*Kras-G12D; Lztr1-KO*) model aligns with the genetic alterations found in human lung cancer. We observed about 50% suppression of *Lztr1* in sorted lung tumor cells isolated from either *Lztr1*-Het or *Lztr1*-KO mice after *Sftpc-Cre* recombinase-coding adenovirus injection (Fig. 1I and Supplementary Fig. S1E). This partial loss of LZTR1 could be due to partial Cre recombination upon intratracheal adenoviral injection, which is in line with the previous reports^{24,25}. Nonetheless, this degree of suppression recapitulated the *LZTR1* haploinsufficiency observed in human LUAD (Supplementary Fig. S1D). Whereas Cre-mediated recombination induced KRAS-G12D expression, LZTR1 suppression did not alter the levels of mutant KRAS (Fig. 1I). In contrast, LZTR1 loss led to increased levels of total KRAS, suggesting alterations of WT-KRAS protein levels (Fig. 1I). Furthermore, TMT-labeled proteomic analysis of sorted lung tumor cells revealed a significant increase in KRAS protein expression (Fig. 1J), without observing any changes in *Kras* mRNA levels (Supplementary Fig. S1F). Moreover, we also did not observe any significant upregulation of other RAS proteins in our mouse model (Fig. 1J). Thus, this model enabled us to investigate a physiologically relevant increase in WT-KRAS level mediated by dysregulation of LZTR1-mediated proteostasis.

Micro-CT-based analysis of tumor growth revealed an increase in tumor burden in *Lztr1*-HET mice (Fig. 1K). Hematoxylin-eosin (H&E) staining showed that lesions appeared in *Lztr1*-HET lungs at an earlier stage and progressed rapidly into larger, compacted adenoma nodules (Fig. 1L). Immunohistochemical analysis of the lung tissue revealed that the tumor lesions were positive for GATA binding protein 6 (GATA6), cytokeratin 19 (CK19), and transcription termination factor 1 (TTF1) (Supplementary Fig. S1G), recapitulating the characteristics of human papillary lung adenocarcinoma. Altogether, these results demonstrate



that elevated KRAS protein levels, resulting from either WT-KRAS overexpression or impaired LZTR1-mediated degradation, accelerate KRAS-driven lung adenocarcinoma progression *in vivo*.

RAS inhibitors impair LZTR1-mediated RAS degradation

The pivotal role of WT-KRAS protein dosage in tumor development suggests that dysregulation of KRAS proteostasis might also affect

therapeutic response. Pan-RAS inhibitors, such as RMC7977, enhance the intrinsic GTPase activity of oncogenic KRAS, thereby shifting it toward its inactive conformation²⁶. Similarly, MRTX1133 stabilizes KRAS in the GDP-bound state²⁷. Given that LZTR1 is known to mediate the degradation of GDP-bound RAS, it is plausible that LZTR1 could contribute to the tumor-suppressive effects of these inhibitors by promoting the degradation of inactive KRAS. However, we observed

Fig. 1 | LZTR1 loss facilitates KRAS-driven lung tumorigenesis. **A, B** Hemalum eosin and Immunostaining analysis of KRAS-G12D and HA (corresponding to KRAS-WT overexpression) of lung tumor sections from the *Kras-G12D; GFP* and *Kras-G12D; WT-KRAS-OE* mice 10 weeks post-Cre injection. Scale bar, 50 μ m. **C** Tumor nodule growth was assessed by tumor volumetric analysis of micro-CT scans in the indicated mice. Data are shown as mean \pm SEM; n = 5 mice per group with p -value calculated by two-sided mixed model analysis with no adjustments. **D** Survival analysis in the indicated mice; n = 5 mice per group with p -value calculated using the Log-rank (Mantel-Cox) test. **E** Heatmaps illustrating the proximity-based interaction signals of KRAS proteins determined by BioID analysis. The data were extracted from^{22,23}. **F** Relative GPS-based stability of KRAS proteins in HEK293T cells expressing shGFP or shLZTR1. Data are shown as mean \pm SEM, n = 4 technical replicates per group. **G** Immunoblot analysis of the indicated proteins in A427 and H727 cells expressing shGFP or shLZTR1. The samples derive from the same experiment. LZTR1, KRAS-G12V, and Vinculin were detected on the same gel; total KRAS was run on a separate gel processed in parallel. Data are shown as mean \pm

SEM, n = 4 technical replicates per group. **H** KRAS mutations and LZTR1 alterations in the TCGA LUAD dataset obtained from cBioPortal. Homdel, homozygous deletion; hetloss, shallow deletion. n = 507 patients with co-occurrence q -value calculated. **I** Immunoblot analysis of the indicated proteins in lung tumor cells isolated from individual mice at 14 weeks post-Cre injection. The samples derive from the same experiment. LZTR1, KRAS-G12D, and Vinculin were detected on the same gel; total KRAS was run on a separate gel processed in parallel. Data are shown as mean \pm SEM, n = 4 mice per group with p -values calculated by two-sided Mann-Whitney test. **J** Expression of RAS proteins in lung cancer cells isolated from the indicated mice by TMT-labeled MS proteomics. Data are shown as mean \pm SEM, n = 4 mice per group with p -values calculated by two-sided Mann-Whitney test. **K** Tumor nodule growth was assessed by tumor volumetric analysis of micro-CT scans. Data are shown as mean \pm SEM; n = 12 mice per group with p -value calculated by two-sided mixed model analysis with no adjustments. **L** H&E staining of the lung tissues from the indicated mice at 6 and 14 weeks post-Cre injection. Scale bar, 100 μ m.

that RMC7977 treatment resulted in a significant accumulation of KRAS, whereas MRTX1133 treatment only caused a modest increase in KRAS protein levels (Fig. 2A, B). Concordantly, the GPS assay demonstrated that treatment with either RMC7977 or MRTX1133 led to WT-KRAS stabilization in an LZTR1-dependent manner (Fig. 2C, D).

A previous study identified the Switch I region of KRAS as a critical determinant for CRL (Cullin 3-RING Ligase)-mediated degradation²⁶ (Fig. 2E). Specifically, the differential stability (deltaPsi) of KRAS-derived peptides in HEK293T cells treated with DMSO or the CRL inhibitor MLN4924 was assessed using a peptide tiling library cloned into the GPS reporter system. This approach revealed that Switch I was particularly susceptible to CRL-mediated degradation, suggesting that Switch I plays a crucial role in LZTR1-mediated degradation. RMC7977 directly binds to the Switch I region, while MRTX1133 induces conformational changes that propagate toward this domain²⁸. A recent structural study solved crystal structures of the LZTR1 Kelch domain bound to KRAS, revealing that the LZTR1-KRAS interface involves loops adjacent to and including portions of the Switch I region²⁹. Altogether, this strongly indicates that both compounds impaired LZTR1-mediated degradation of KRAS.

Notably, RMC7977 treatment completely abrogated the difference in KRAS expression levels between shGFP- and shLZTR1-expressing cells, whereas MRTX1133 only partially mitigated this difference (Fig. 2A-D). Consistently, RMC7977 induced comparable growth inhibition in shGFP- and shLZTR1-expressing cells (Fig. 2F). In contrast, LZTR1 knockdown in KRAS-G12D-mutant A427 lung cancer cells impaired their response to MRTX1133 treatment (Fig. 2G), highlighting the impact of WT-KRAS protein levels in modulating drug response. The reduced drug sensitivity observed in LZTR1-depleted cells was reversed upon re-expression of GFP-tagged-LZTR1 (Fig. 2G, H).

We further assessed the impact of LZTR1 loss on the response to MRTX1133 in vivo. We found that, whereas MRTX1133 treatment dramatically suppressed the growth of *Kras-G12D; Lztr1-WT* tumors, it only modestly delayed the growth of *Kras-G12D; Lztr1-HET* tumors at earlier stages, with little to no significant effect at later time points (Fig. 2I). These results suggest that LZTR1-mediated proteostatic regulation of RAS proteins might affect the efficacy of RAS inhibitors, whereas LZTR1 downregulation in human cancer could be a common mechanism of intrinsic resistance to RAS inhibitors.

Increased levels of WT-RAS protein activate the mTOR/HIF1 α axis

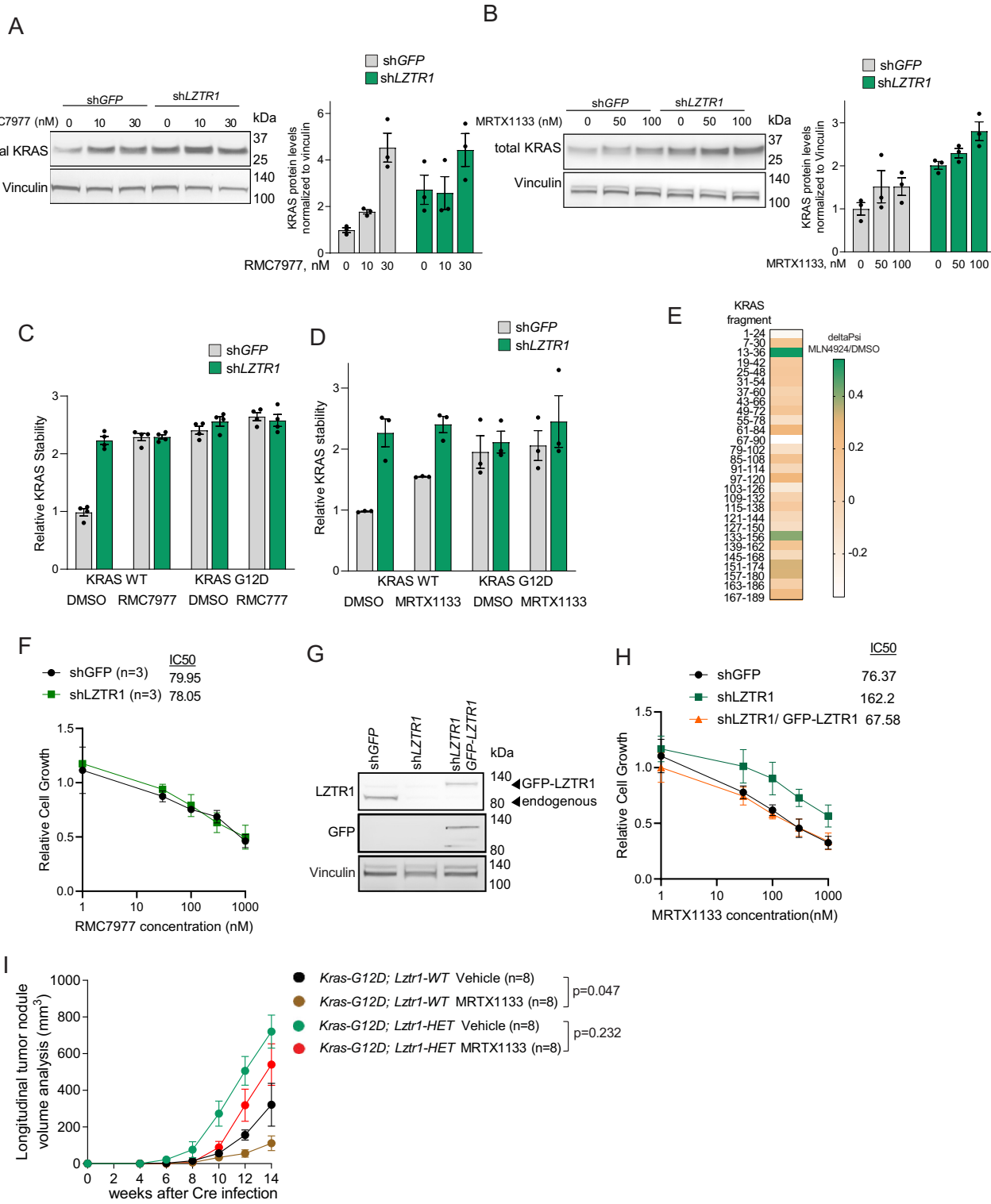
We next explored the mechanism by which increased WT-KRAS protein levels contribute to RAS inhibitor resistance. A gene set enrichment analysis (GSEA) of KRAS-mutant TCGA LUAD samples revealed that LZTR1 loss was associated with altered gene expression signatures linked to the mTOR pathway and hypoxia-related signaling, a transcriptional program downstream of mTOR⁵ (Fig. 3A). Proteomic and

phosphoproteomic analyses of human lung cancer cells showed that mTOR signaling was one of the most significantly altered pathways upon LZTR1 knockdown (Fig. 3B, C; Supplementary Data 1-3). Consistently, LZTR1 suppression promoted mTOR re-localization to lysosomes, as evidenced by increased co-localization with the lysosomal marker LAMP1 (Fig. 3D). This was accompanied by elevated phosphorylation of canonical mTOR targets, p70 S6K (70 kDa Ribosomal Protein S6 Kinase) and 4EBP1 (Eukaryotic Translation Initiation Factor 4E Binding Protein 1) (Fig. 3E). The activation of p70 S6K in cells depleted for LZTR1 was rescued by restoring LZTR1 expression (Fig. 3F). In line with mTOR activation, LZTR1 depletion also led to increased mRNA expression and elevated secretion of vascular endothelial growth factor A (VEGFA), a key target of the hypoxic response (Fig. 3G, H).

Proteomic and immunoblotting analyses of lung tumor cells isolated from *Lztr1-WT* and *Lztr1-HET* mice also revealed upregulation of mTOR signaling in the *Lztr1-HET* tumors (Fig. 4A, Supplementary Fig. S2A and Supplementary Data 1-3). Proximity ligation assay (PLA) analysis showed increased interaction between LAMP1 and mTOR in *Lztr1-HET* lung tumors, further indicating enhanced mTOR activity upon *Lztr1* loss (Fig. 4B and Supplementary Fig. S2B). *Lztr1* haploinsufficient tumors also exhibited elevated HIF1 α nuclear immunostaining (Fig. 4C), while ELISA-based cytokine array analysis demonstrated increased VEGFA secretion in the supernatant of *Lztr1-HET* lung tumor cells (Fig. 4D). Optical tomography (OPT) of cleared lungs also revealed a significant difference in the blood vessel architecture between *Kras-G12D; Lztr1-HET* and *Kras-G12D; Lztr1-WT* tumors. In *Lztr1-WT* mice, the vasculature surrounding the tumors was organized, with larger vessels branching into smaller ones in a hierarchical pattern. In contrast, in *Lztr1-HET* mice, the tumor-associated blood vessels were disorganized and lacked a conventional hierarchy, as quantified by vascular tortuosity (Supplementary Fig. S2C). Moreover, the FITC-dextran diffusion assay indicated leaky vessels adjacent to the *Lztr1-HET* tumors (Supplementary Fig. S2C).

In the *Kras-G12D; WT-Kras* model, elevated KRAS-WT protein levels also promoted increased mTOR activity, as indicated by higher phosphorylation of p70S6K (Fig. 4E). Enhanced mTOR signaling was accompanied by increased VEGFA secretion and vascular abnormalities (Fig. 4F and Supplementary Fig. S2D). Collectively, these findings demonstrate that KRAS-WT up-regulation contributes to the activation of the mTOR/HIF1 α signaling axis and subsequent vascular remodeling.

RMC7977 treatment, which induced KRAS-WT overexpression, also led to the activation of mTOR signaling, as evidenced by increased interaction between mTOR and LAMP1, enhanced phosphorylation of mTOR downstream targets, and elevated VEGFA secretion (Fig. 4G-J). In contrast, these effects were significantly reduced in cells lacking LZTR1, in which RMC7977 treatment did not trigger additional mTOR



signaling. This is likely because KRAS degradation was disrupted in these cells, leading to higher baseline levels of KRAS protein (Fig. 4G–J). These findings indicate that either LZTR1 loss or RMC7977 treatment increases KRAS-WT protein levels, thereby promoting mTOR activation and VEGFA upregulation.

Increased wild-type KRAS protein promotes the mTOR via the lysosomal re-localization of the SLC3A2/SLC7A5 complex

We next assessed how elevated KRAS-WT protein levels lead to mTOR activation. Because solute carrier (SLC) transporters regulate amino

acid availability and thereby control mTOR activity, we focused on the function of the SLC3A2/SLC7A5 heterodimer, a major transporter of large neutral amino acids. Proximity-based proteomic analyses showed that both wild-type and oncogenic KRAS bind the SLC3A2/SLC7A5 heterodimer at comparable levels (Fig. 5A, B). Concordantly, SLC7A5 showed comparable co-immunoprecipitation with both WT-KRAS and KRAS-G12D (Supplementary Fig. S3A), indicating that this interaction is independent of KRAS mutational status. We confirmed that mTOR activation and VEGF upregulation following LZTR1 loss relied on SLC3A2/SLC7A5 expression (Fig. 5C–E and

Fig. 2 | RAS inhibitors impair LZTR1-mediated degradation of KRAS.

A Immunoblotting for total KRAS in H727 cells expressing shGFP or shLZTR1 and treated with RMC7977 (10 or 30 nM, 24 h). Vinculin and total KRAS were detected on the same gel. Data are shown as mean \pm SEM, $n = 3$ technical replicates per group. **B** Immunoblotting for total KRAS in A427 cells expressing shGFP or shLZTR1 and treated with MRTX1133 (50 or 100 nM, 24 h). Vinculin and total KRAS were detected on the same gel. Data are shown as mean \pm SEM, $n = 3$ technical replicates per group. **C** GPS-determined stability of wild-type and mutant KRAS in HEK293T cells expressing shGFP or shLZTR1 and treated with RMC7977 (30 nM, 24 h). Data are shown as mean \pm SEM, $n = 4$ technical replicates per group, with p -value calculated by two-sided mixed model analysis with no adjustments. **D** GPS-based stability of wild-type and mutant KRAS in HEK293T cells expressing shGFP or shLZTR1 and treated with MRTX1133 (100 nM, 24 h). Data are shown as mean \pm SEM, $N = 4$ technical replicates per group. **E** GPS-based stability of KRAS-derived peptides

assessed in DMSO- or MLN4924-treated HEK293T cells. The heatmap was generated using deltaPsi scores obtained from ref. 26. **F** The IC50 of RMC7977 was measured by monitoring the growth of A427 cells expressing shGFP or shLZTR1 using Incucyte. Data are presented as means \pm SEM; $n = 3$ technical replicates per group. **G** Immunoblotting for GFP and LZTR1 in A427 cells expressing shGFP or shLZTR1 and GFP-LZTR1. LZTR1, GFP, and Vinculin were detected on the same gel. **H** The IC50 of MRTX1133 was measured by monitoring the growth of A427 cells expressing shGFP or shLZTR1 using Incucyte. Data are presented as mean \pm SEM, $n = 3$ technical replicates. **I** Tumor nodule growth was assessed by tumor volumetric analysis of micro-CT scans. Mice were treated with vehicle or MRTX1133 (10 mg/kg, IP every 2 days). Data are shown as mean \pm SEM; $n = 8$ mice per group with p -value calculated using the two-sided mixed model analysis with no adjustments.

Supplementary Fig. S3B), confirming that LZTR1 can modulate mTOR signaling through the SLC3A2/SLC7A5 complex.

Previous studies have indicated that RAS signaling can increase the expression of certain SLC transporters³⁰, we did not detect any changes in SLC3A2 or SLC7A5 expression in cells with LZTR1 depletion or upon treatment with RMC7977 (Fig. 5F). Consistently, amino acid uptake and secretion were comparable between shGFP and shLZTR1 cells, indicating that LZTR1 does not regulate amino acid transport at the plasma membrane (Supplementary Fig. S2E, F). On the other hand, a recent study demonstrated that KRAS can organize a signaling complex with the amino acid transporter, SLC3A2/SLC7A5, and mTOR on endolysosomes, which directly activates mTORC1³¹. Lysosome-IP analysis revealed that elevated KRAS levels increased the recruitment of both the SLC3A2/SLC7A5 complex and mTOR to LAMP1-positive endolysosomal membranes (Fig. 5G). We also observed heightened colocalization of SLC3A2 with the lysosomal marker LAMP1 in lung cancer cells either depleted of LZTR1 or treated with RMC7977 (Fig. 5H).

This suggests that high levels of WT-KRAS could promote mTOR activation by driving endocytic delivery of the SLC3A2/SLC7A5 complex to the endolysosome. In agreement with this idea, we found that the pharmacological inhibition of endocytic trafficking to the lysosome using Dyngo-4a³² eliminated the difference in p70S6K phosphorylation downstream of mTOR between shGFP and shLZTR1 expressing cells (Supplementary Fig. S3C). Once re-localized on lysosomes, the SLC3A2/SLC7A5 heterodimer triggers exchange of intralysosomal glutamine for extracellular leucine, inducing mTOR re-localization on endolysosomes and its activation^{33,34}. Proximity between mTOR and SLC3A2 was confirmed in lung cancer cells with depleted LZTR1 and in lung tumors from *Lztr1-HET* mice (Fig. 5I, J). Thus, elevated KRAS-WT can induce mTOR signaling through an “in-out” amino-acid delivery pathway that converges on lysosomal nutrient sensing.

Targeting LAT1/mTOR overcomes wild-type KRAS-induced resistance

We next assessed strategies to overcome intrinsic resistance to KRAS inhibitors. Impaired KRAS degradation in LZTR1-deficient cancer cells led to reduced sensitivity to MRTX1133 *in vitro*, indicating a cell-intrinsic resistance mechanism linked to mTOR pathway activation (Fig. 2F, G). *In vivo*, elevated WT-KRAS levels also resulted in altered vascular architecture (Supplementary Fig. S2D), potentially affecting drug delivery. Thus, both tumor-intrinsic and microenvironmental factors could contribute to the limited efficacy of RAS inhibitors. Thus, we investigated the potential of LAT1/mTOR inhibition to address both tumor-intrinsic and vascular aspects of resistance to KRAS inhibitors.

Whereas the KRAS inhibitor MRTX1133 failed to reverse the upregulation of VEGFA secretion in A427 cells, the mTOR inhibitors everolimus or the dual PI3K/mTOR inhibitor dactolisib (NVP-BEZ235) abrogated the VEGFA upregulation (Fig. 6A). In contrast to MRTX1133,

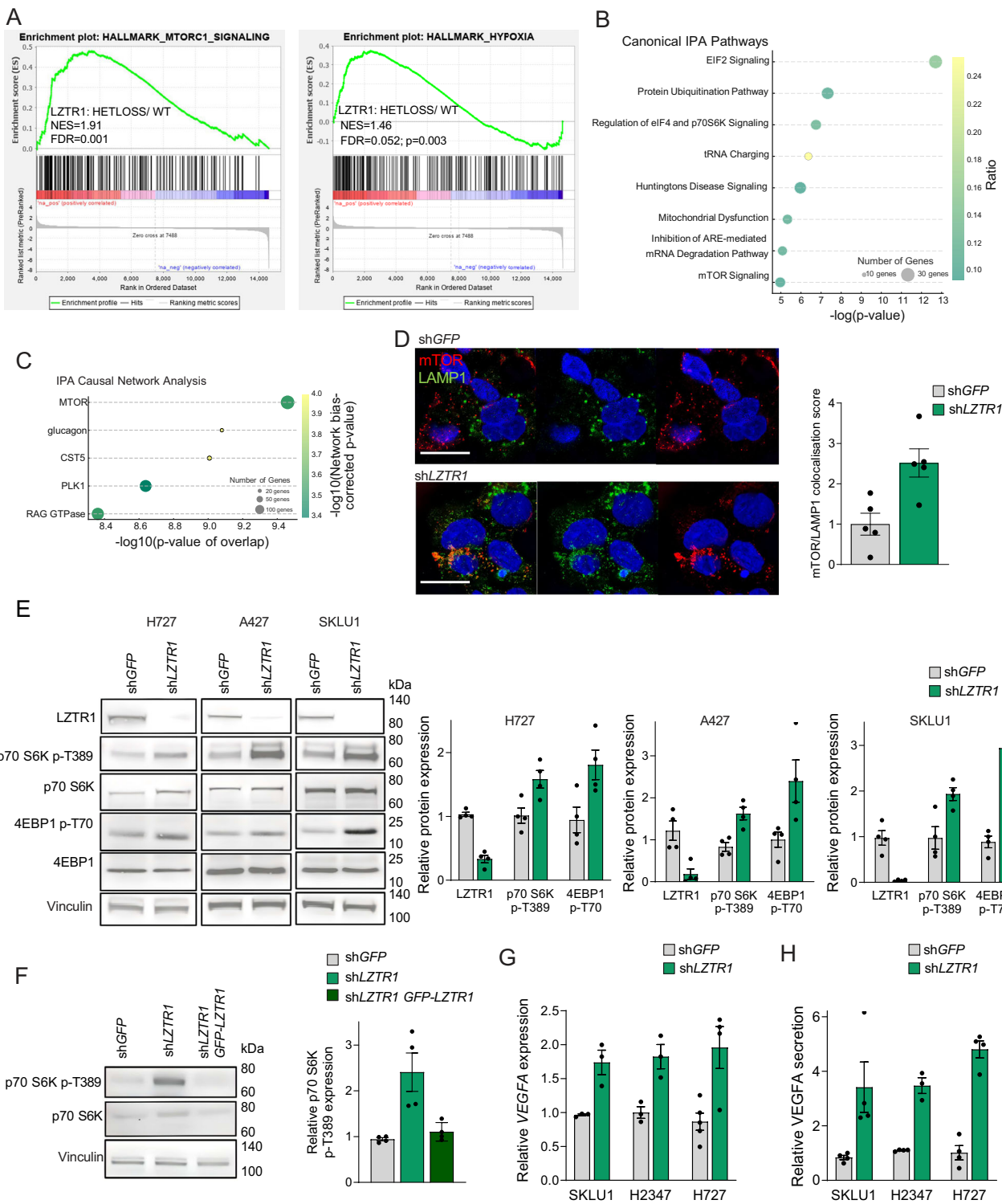
dactolisib treatment also led to a significant reduction in p70 S6K phosphorylation (Fig. 6B), a decrease in HIF1 α nuclear expression, and normalized vasculature in *Lztr1-HET* tumors (Fig. 6C, D). These findings suggest that LZTR1-mediated KRAS stabilization confers resistance to MRTX1133 by promoting mTOR-driven survival signaling and vascular abnormalities, allowing tumors to evade inhibition of KRAS-G12D. In *Kras-G12D; Lztr1-WT* mice, MRTX-1133 monotherapy produced profound and sustained tumor regression, with virtually complete inhibition of growth over the treatment period (Supplementary Fig. S4A). By contrast, *Kras-G12D; Lztr1-HET* tumors showed limited response to MRTX1133 alone, continuing growth despite drug administration. To overcome this resistance, we combined MRTX1133 with dactolisib. This combination not only induced tumor regressions but also prevented rebound growth, producing durable suppression of tumor burden (Fig. 6E). These results indicate that *Lztr1* heterozygosity confers partial resistance to KRAS inhibition, which can be effectively overcome by concurrent blockade of the mTOR axis.

Consistent with the role of the SLC3A2/SLC7A5 amino acid transporter complex in WT-KRAS-driven mTOR activation, pharmacological inhibition of LAT1 using JPH203 blocked phosphorylation of downstream mTOR effectors and increased VEGFA secretion (Supplementary Fig. S3D, E). Similar rescue effects were observed in JPH203-treated lung cancer cells overexpressing KRAS-WT (Supplementary Fig. S3F, G). In the *Kras-G12D; Lztr1-HET* lung cancer model, combining MRTX1133 with JPH203 resulted in sustained tumor growth suppression (Fig. 6F). Importantly, no signs of weight loss were observed during 12 weeks of the combination period with MRTX1133 and either dactolisib or JPH203 (Supplementary Fig. S4B, C), supporting the tolerability of these combination regimens.

We also assessed whether the inhibition of LAT1/mTOR induced by KRAS-WT stabilization sensitizes cancer cells to pan-RAS inhibitor RMC7977. We observed a synergistic interaction in H727 cells when combining RMC7977 with either dactolisib or JPH203. The most pronounced synergy occurred within the concentration range surrounding the IC50 values of both agents, as indicated by the Most Synergistic Area (MSA) analysis (Fig. 6G, H and Supplementary Fig. S5). Together, these findings suggest that pharmacological inhibition of mTOR signaling driven by elevated KRAS-WT protein levels may represent a viable strategy to overcome intrinsic resistance and enhance the therapeutic efficacy of direct RAS inhibitors.

Discussion

Direct RAS inhibitors hold significant therapeutic potential by offering promising treatment strategies for RAS-driven cancers. However, intrinsic resistance to these agents remains a major obstacle. Our study reveals that elevated WT-KRAS protein levels attenuate the efficacy of the KRAS G12D-specific inhibitor MRTX1133 in tumors with LZTR1 downregulation, an alteration observed in approximately 40% of lung adenocarcinoma patients. This increase in KRAS protein abundance results from impaired LZTR1-mediated degradation and is similarly



induced by treatment with the cyclophilin A–based pan-RAS inhibitor RMC7977. In both contexts, the stabilization of WT-RAS proteins leads to paradoxical activation of the pro-survival mTOR/HIF1 α pathway.

These findings challenge the longstanding paradigm that WT-KRAS functions solely as a tumor suppressor³⁵. Instead, here we demonstrate that increased WT-KRAS dosage exerts pro-tumorigenic effects, in part by sustaining mTOR-driven survival signaling. Notably, prior models of KRAS-driven oncogenesis have primarily focused on genetic modulation of the mutant allele, without assessing WT and mutant KRAS protein expression levels¹⁴. Our data strongly indicate that elevated WT-KRAS protein levels can functionally antagonize the

therapeutic efficacy of allele-specific inhibitors both *in vitro* and *in vivo* due to the pro-survival effect of mTOR activation. *In vivo* resistance may be further amplified by tumor vascular remodeling.

The contribution of LZTR1-mediated increased dosage of WT-KRAS protein to resistant phenotypes aligns with recent studies demonstrating that both mutant-specific and pan-KRAS inhibitors often have limited impact due to compensatory activation of wild-type RAS-like GTPases^{36–39}. The regulatory role of LZTR1 in modulating the ubiquitination of different RAS family members is well-established^{16–18,40,41}. However, here we focused on the effects on KRAS stabilization, as KRAS is the most highly expressed isoform in

Fig. 3 | LZTR1 loss activates the mTOR/HIF1α/VEGFA axis. **A** GSEAs were performed on TCGA LUAD samples with different *LZTR1* statuses. Patients with Hetloss or shallow deletion for *LZTR1* were compared to WT patients. $N = 82$ and 75 patients, respectively. **B** Canonical pathway analysis of Ingenuity Pathway Analysis (IPA) of differentially expressed proteins in H727 cells expressing shGFP or sh*LZTR1* identified by TMT-labeled MS proteomics; $n = 3$ technical replicates per group. **C** Causal network IPA analysis of differentially phosphorylated proteins in H727 cells expressing shGFP or sh*LZTR1* identified by Ti-IMAC-enriched phosphoproteomic analysis; $n = 3$ technical replicates per group. **D** Immunofluorescence analysis for LAMP1 and mTOR in H727 cells expressing shGFP or sh*LZTR1*. Scale bar $20 \mu\text{m}$. Colocalization score quantification is shown as mean \pm SEM; $n = 5$ technical replicates per group. **E** Immunoblot analysis of the same indicated proteins in

human lung cancer cells expressing shGFP or sh*LZTR1*. LZTR1, p70 S6K p-T389, 4EBP1 p-T70 and Vinculin were detected on the same gel, but different gels for total p70 S6K and 4EBP1 that were processed in parallel. The immunoblot quantification is shown as mean \pm SEM; $n = 4$ technical replicates per group. **F** Immunoblotting for phosphorylated and total p70 S6K in the indicated A427 cells. p70 S6K p-T389 and Vinculin were detected on the gel, but different gels for total p70 S6K that was processed in parallel. Data are shown as mean \pm SEM, $n = 4$ technical replicates per group (**G**) RT-qPCR analysis of *VEGFA* expression in lung cancer cells expressing shGFP or sh*LZTR1*. Data are shown as mean \pm SEM; $n = 4$ technical replicates per group. **H** ELISA-based analysis of VEGFA levels in the supernatant of lung cancer cells expressing the indicated constructs. Data are shown as mean \pm SEM; $n = 4$ technical replicates per group.

lung tissue⁴². We also did not observe an accumulation of RIT1, a well-recognized substrate of LZTR1⁴⁰, upon LZTR1 depletion in our models, suggesting that the LZTR1-mediated effect could be tissue-specific. However, when considering the high heterogeneity of lung adenocarcinomas, we could not exclude that other RAS family members contribute to the observed phenotypes. This suggests that targeting KRAS degradation with recently developed PROTACs targeting KRAS⁴³ may be insufficient to suppress mTOR activation.

Our results suggest that LZTR1 could act as a haploinsufficient tumor suppressor in the context of KRAS-mutant lung cancer. Recent studies have demonstrated that another CUL3 substrate adapter, SPOP, forms high-order oligomers in a concentration-dependent manner⁴⁴. SPOP oligomerizes in the presence of BTB-BACK domains, which resemble the ones present in LZTR1. Similar to SPOP, WT-LZTR1 can form multimers and show punctate immunostaining, whereas disease-associated LZTR1 BTB-BACK domain mutants, which are unable to form multimers and ubiquitinate RAS proteins, show a dispersed cytoplasmic localization^{17,45}. Thus, we speculated that decreased LZTR1 expression due to the loss of one *LZTR1* allele might affect oligomer formation, abrogating its ability to ubiquitinate KRAS. These findings suggest that the shallow deletion of *LZTR1* observed in approximately 40% of KRAS-mutant LUADs results in a full loss of function and could lead to intrinsic resistance to RAS inhibition.

Previous studies demonstrated that resistance to RAS inhibitors could be overcome by inhibiting SHP2 or EGFR, which block the activation of wild-type RAS isoforms. However, given that *LZTR1* loss also confers resistance to RTK and SHP2 inhibitors^{18,20,21}, these approaches may be inadequate in tumors with *LZTR1* loss. Restoring LZTR1 function could offer a more effective strategy to block compensatory WT-RAS activation following initial KRAS inhibition. Another option could be to inhibit the SLC3A2/SLC7A5-mTOR axis. Inhibiting SLC3A2/SLC7A5 or mTOR activity not only directly suppresses tumor growth but also impacts the tumor-associated endothelium⁴⁶, thus enhancing the overall therapeutic effect. The combination of RAS inhibitors with mTOR inhibitors like dactolisib, or the LAT1 inhibitor JPH203, demonstrated strong therapeutic potential, with no signs of toxicity observed during the monitoring phase. Other mTOR inhibitors, such as sirolimus or everolimus, which have distinct pharmacodynamic properties compared to those tested here, could also be explored for their potential synergistic effects.

In summary, our findings uncover an intrinsic resistance mechanism in KRAS-mutant lung cancer, whereby stabilization of WT-RAS due to genetic or pharmacological perturbation undermines the clinical benefit of RAS-targeted therapies, posing a significant challenge for the treatment of KRAS-mutant cancers. These results underscore the need to consider proteostatic regulation of RAS proteins in the development and deployment of next-generation RAS inhibitors. Alternative approaches include developing targeted RAS degraders or LZTR1 activators, which could mitigate increased RAS protein levels and mTOR pathway activation.

Materials and methods

Genetically modified mice

All procedures involving animals were performed in accordance with the guidelines of the IACUC of KU Leuven and approved project P203/2020. The animal studies were carried on mice, strain C57BL6/J b, only on males, that were used between 4 weeks and 18 weeks of age. The maximal tumor burden permitted by the ethics committee is 2000 mm³, and this maximal tumor burden was not exceeded.

To generate the genetically engineered mice, *Lztr1^{tm1a}(EUCOMM)^{Wtsi}* embryonic stem cells were purchased from EUCOMM (EPD0140_5_E07, EPD0140_5_G06) and used for in vitro fertilization of female CD-1 cells. The primers used for genotyping were as follows:

Sequence			
<i>neo</i>	Forward	5'-AAGATGGATTGCACGCAGGTTCTC-3'	
	Reverse	5'-GACGA-GATCCTGCCGTCGGGCATGCCGCC-3'	
<i>Lztr1</i>	Forward	5'-AGGTGAGGGTAGAGGAAGC-3'	
	Reverse	5'-TTTCTGACCCAACCTCCAAAG-3'	

Lztr1^{fl/fl} mice (*Lztr1^{tm1c}(EUCOMM)^{Wtsi}*) were generated by flipase-mediated recombination by breeding *Lztr1^{tm1a}(EUCOMM)^{Wtsi}* mice with *Gt(ROSA)26Sortm1(FLP1)Dym* 1 mice. *Lztr1^{fl/fl}* mice were subsequently backcrossed on C57BL6/J background with *B6.129S4-Krastm4Tyr/J (LSL-Kras^{G12D}; RRID:IMSRJAX:008179)* using the project “CreationSablina2020” in accordance with the guidelines of the IACUC of KU Leuven. Interbred *Kras G12D^{sl/slt}*, *Lztr1^{fl/fl}* mice exhibited normal development, were viable and fertile, and were bred on the “GS2 breeding Sablina” project. Naïve mice showed no disease or pain phenotypes. Prof. Anna Sablina is the owner of the mice, according to the MTAs signed by EUCOMM and the Jackson Laboratory.

Plasmids

Plasmid name	Source
MSCV-CMV-DsRed-IRES-EGFP DEST	Addgene plasmid #41941
pDONR223-KRAS4B	Addgene plasmid #81751
pDONR223-KRAS4B G12V	Addgene plasmid #81665
pDONR223-KRAS4B G12D	Addgene plasmid #81651
pDONR223-KRAS4B G13D	Addgene plasmid #82808
pDONR223-KRAS4B G12C	Addgene plasmid #81667
pLenti CMV DsRed IRES GFP KRAS4B WT	Gateway recombination

pLenti CMV DsRed IRES GFP KRAS4B G12D	Gateway recombination
pLenti CMV DsRed IRES GFP KRAS4B G12C	Gateway recombination
pLenti CMV DsRed IRES GFP KRAS4B G12V	Gateway recombination
pLenti CMV DsRed IRES GFP KRAS4B G13D	Gateway recombination
pMT107-6xHis-ubiquitin	a gift from Dr. Bohmann (University of Rochester, USA)
shRNA targeting GFP generated by the RNAi Consortium (TRC)	TRCN0000072178
SLC3A2 Sigma Mission shRNAs generated by the RNAi Consortium (TRC)	TRCN0000043383 TRCN0000043384 TRCN0000043386
SLC7A5 Sigma Mission shRNAs generated by the RNAi Consortium (TRC)	TRCN0000043008 TRCN0000043009 TRCN0000043010
LZTR1 shRNAs generated by the RNAi Consortium	TRCN0000240480 TRCN0000181026
pLJC6-3XHA-TMEM192	Addgene #104434
pLA CMV HA LZTR1 WT	Generated as described in ref. 17
pLA CMV GFP LZTR1 WT	Generated as described in ref. 17
pLV-SPB > HA-mKras4B:IRES:Cre	Generated by VectorBuilder
pLV-SPB > EGFP:IRES:Cre	Generated by VectorBuilder
pTwist Flag KRAS4B WT	Generated by Twist Bioscience
pTwist Flag KRAS4B G12D	Generated by Twist Bioscience

All plasmids were verified using DNA sequencing (Eurofins Genomics).

MSCV-CMV-DsRed-IRES-EGFP-DEST was gift from Stephen Elledge; pDONR223-KRAS4B plasmids was gift from Jesse Boehm, William Hahn & David Root; pLJC6-3XHA-TMEM192 was gift from David S. Sabatini.

Cell lines and reagents

EPCAM-positive cells were isolated from mouse lung tumors after homogenization and digestion using the Multi Tissue Dissociation Kit 2 (Miltenyi Biotech). The digested mix of cells was first incubated with anti-CD45 beads to remove CD45-positive cells and then isolated with anti-EPCAM magnetic beads (Miltenyi Biotech). The quality of each fraction was evaluated using immunostaining or immunoblotting for CD45, pan-cytokeratin, and EPCAM.

Lentiviral infection was performed as described by the RNAi Consortium (TRC). Infected cells were selected using puromycin for three days (2 µg/ml, InvivoGen) or hygromycin B for seven days (500 µg/ml, InvivoGen). Cells were transfected using GeneJuice (Merck) or Lipofectamine 3000 (Thermo Fisher Scientific).

Cell growth was measured with the real-time monitoring system, Incucyte (Essen Bioscience). A total of 5000 cells were plated in a 96-well plate in triplicate, and the cell index was measured in at least three independent experiments.

Drugs were purchased from MedChemExpress and used at the dose indicated below:

	In vitro	In vivo
MRTX1133	1–200 nM	10 mg/kg
Dactolisib (NVP BEZ 235)	1 µM	10 mg/kg
Dyngo4a (hydroxydynasore)	10 µM	–
Everolimus	1 µM	–
JPH203	1 µM	10 mg/kg
RMC7977	1–100 nM	–

Amino acids uptake and secretion measurements

Cells were cultured in standard growth medium lacking GlutaMAX supplemented with 5% FBS and 1× penicillin–streptomycin (P/S). To establish baseline metabolite levels, fresh medium (without FBS or P/S) was collected at the start of the experiment. Conditioned medium was sampled in parallel with cell-free control wells.

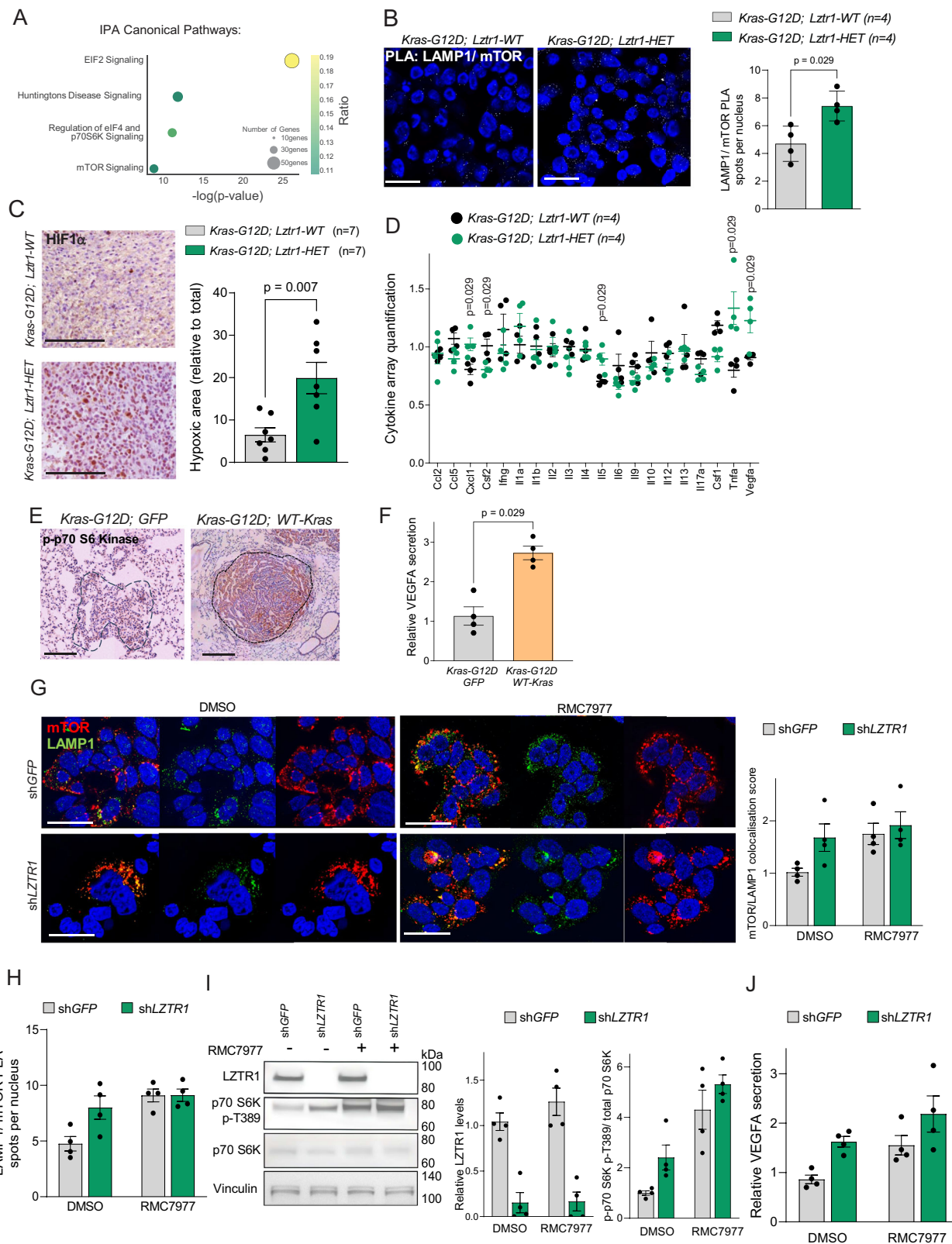
Metabolites were extracted from 20 µL medium using 500 µL chloroform and 800 µL MeOH/H2O (5:3, v:v) containing 0.5 µg/ml glutarate and norvaline as internal standards. Next, samples were shaken and centrifuged to separate the polar and non-polar phase. The polar MeOH/H2O phase was transferred and dried overnight under vacuum at 4 °C. Subsequently, samples were resuspended in 50 µL 80% methanol in water.

For the analysis of media samples by LC-MS, a 1290 Infinity II liquid chromatography (Agilent Technologies) with a thermal autosampler set at 4 °C, coupled to a Q-TOF 6546 mass spectrometer (Agilent Technologies) was used. 5 µL sample was injected into an InfinityLab Poroshell 120 HILIC-Z, 2.1 × 150 mm, 2.7 µm (Agilent Technologies). The separation of metabolites was achieved using a gradient for 32 min at 50 °C with a flow rate of 0.25 ml/min (solvent A: 10 mM ammonium acetate (pH 9) in water; solvent B: 10 mM ammonium acetate (pH 9) in 85% acetonitrile; 0 min: 4% A, 2 min: 4% A, 5.5 min: 12% A, 8.5 min: 12% A, 9 min: 14% A, 14 min: 14% A, 19 min: 18% A, 25 min: 35% A, 27 min: 35% A, 28 min: 4% A, 32 min: 4% A). The MS operated in negative mode (m/z range: 50–1200) using a sheath gas temperature of 350 °C (12 L/min) and a gas temperature at 225 °C (13 L/min). The nebulizer was set at 35 psi, the fragmentor at 125 V, and the capillary at 3500 V.

Data was analyzed using the MassHunter Profiler software (Agilent Technologies, version 10.0) and normalized by the internal standard. To quantify absolute metabolite concentrations, a standard curve for each metabolite was used. Standards were extracted and analyzed in parallel to the other samples. Specific uptake or secretion rates (q) were calculated as $(\Delta\text{metabolite} \times \text{growth rate})/\Delta\text{cell number}$, where $\Delta\text{metabolite} = (\text{metabolite concentration} - \text{blank})$.

Intratracheal Adenoviral injection

The Adenovirus expressing Cre recombinase under the Surfactant Protein C (*Sftpc*) promoter was purchased from The University of Iowa Gene Transfer Vector Core (<https://vector-core.medicine.uiowa.edu/collections/ad5/products/ad5mspc-cre>). The virus was added to MEM and prepared in a sterile syringe with a 23–20-gauge tracheal tubing or a 22-gauge venous catheter. The injected volume was ~0.05 ml. Mice were anesthetized using an appropriate method, such as an intraperitoneal injection of ketamine and xylazine. The mouse was placed in the prone position on a surgical platform. The neck region of each mouse was exposed and disinfected using povidone-iodine. A small incision was made in the skin and subcutaneous tissue to expose the trachea. Alternatively, a non-invasive method that did not require an incision was used, such as inserting the tubing through the mouth and into the trachea. The tubing was carefully inserted into the trachea to prevent damage to the surrounding tissues. The substance was slowly injected into the trachea to prevent leakage and reflux. The chest movements of mice were monitored to confirm that the substance had



reached the lungs. The tubing was withdrawn, and the incision was closed with sutures. The mice were monitored until they recovered from anesthesia, and analgesia was provided if needed.

Computed micro-computed tomography (micro-CT)

Before the start of the imaging sessions, the animals underwent at least one week of acclimatization to the new environment. The

animals were anesthetized using isoflurane (induction at 3% in 100% oxygen and maintenance at 1-2% in 100% oxygen). The animals were scanned using a dedicated *in vivo* micro-CT scanner (SkyScan 1278, Bruker micro-CT, Kontich, Belgium) at an X-ray dose that was well tolerated⁴⁷⁻⁴⁹. The images were acquired with the following parameters: 65 kVp X-ray source voltage and 350 μ A current combined with an X-ray filter of 1 mm aluminum, 150 ms exposure time per

Fig. 4 | *Lztr1* loss in *KRAS*-mutant tumors drives activation of the mTOR/HIF1α pathway. **A** Canonical pathway IPA analysis of differentially expressed proteins in lung cancer cells isolated from the indicated mice, identified by TMT-labeled MS proteomics. $n = 3$ mice per group. **B** PLA was performed on lung adenoma nodules using antibodies against LAMP1 and mTOR. The number of PLA puncta, indicative of LAMP1/mTOR proximity, was quantified per nucleus. $n = 4$ mice per group, p -value calculated by two-sided Mann-Whitney analysis. Scale bar 20 μ m. **C** Immunostaining analysis of HIF1α in lung adenoma nodules at 14 weeks post-Cre injection. Scale bar 30 μ m. $n = 7$ mice per group with a minimum of 8 tumor lesions analyzed per mouse, p -value calculated by two-sided Mann-Whitney analysis. **D** ELISA-based cytokine analysis in supernatants of lung tumor cells isolated from the indicated mice 14 weeks post-Cre injection. $n = 4$ mice per group, p -value calculated by two-sided Mann-Whitney analysis. **E** Immunostaining analysis of phosphorylated p70 S6K in lung tumor sections at 10 weeks post-Cre injection. Scale bar 100 μ m. **F** ELISA-based analysis of VEGFA levels in the supernatant of isolated tumor cells from mice. $n = 4$ mice per group, p -value calculated by two-sided Mann-Whitney analysis without adjustments. **G** Immunofluorescence analysis using antibodies against LAMP1 and mTOR in H727 cells expressing shGFP or shLZTR1 treated with RMC7977 (10 nM, 24 h) or DMSO. Colocalization score is shown as mean \pm SEM. $n = 4$ technical replicates. Scale bar 20 μ m. **H** PLA was performed on H727 cells expressing shGFP or shLZTR1 using antibodies against LAMP1 and mTOR. The number of PLA puncta, indicative of LAMP1/mTOR proximity, was quantified per nucleus. $n = 4$ technical replicates per group. **I** Immunoblot analysis of phosphorylated and total p70 S6K in H727 cells expressing shGFP or shLZTR1. LZTR1, p70 S6K p-T389 and Vinculin were detected on the same gel, but different gels for total p70 S6K that was processed in parallel. Normalization with Vinculin. $N = 4$ technical replicates. **J** ELISA-measured VEGFA levels in the supernatant of H727 cells treated with DMSO or RMC7977 (10 nM, 24 h). $n = 4$ technical replicates per group.

100 μ m. **F** ELISA-based analysis of VEGFA levels in the supernatant of isolated tumor cells from mice. $n = 4$ mice per group, p -value calculated by two-sided Mann-Whitney analysis without adjustments. **G** Immunofluorescence analysis using antibodies against LAMP1 and mTOR in H727 cells expressing shGFP or shLZTR1 treated with RMC7977 (10 nM, 24 h) or DMSO. Colocalization score is shown as mean \pm SEM. $n = 4$ technical replicates. Scale bar 20 μ m. **H** PLA was performed on H727 cells expressing shGFP or shLZTR1 using antibodies against LAMP1 and mTOR. The number of PLA puncta, indicative of LAMP1/mTOR proximity, was quantified per nucleus. $n = 4$ technical replicates per group. **I** Immunoblot analysis of phosphorylated and total p70 S6K in H727 cells expressing shGFP or shLZTR1. LZTR1, p70 S6K p-T389 and Vinculin were detected on the same gel, but different gels for total p70 S6K that was processed in parallel. Normalization with Vinculin. $N = 4$ technical replicates. **J** ELISA-measured VEGFA levels in the supernatant of H727 cells treated with DMSO or RMC7977 (10 nM, 24 h). $n = 4$ technical replicates per group.

projection, three projections averaged per view, acquiring projections with 0.9° increments over a total angle of 220°, producing reconstructed 3D datasets with a 50 μ m isotropic reconstructed voxel size. The total scanning time per mouse was approximately 2.5 min, resulting in a measured delivered radiation dose of approximately 60–80 mGy per scan. A baseline scan was performed before the adenoviral injection, and four weeks after the injection, scans were performed every two weeks. The total nodule volume was evaluated after segmentation of the lung using MIPAV (NIH). Next, each region was analyzed to extract features, such as shape, texture, and intensity, which can help identify the nodules. The nodules were then separated from the blood vessels using a mathematical formula called the sphericity parameter, which measures the sphericity of an object. The more spherical an object is, the more likely it is that it is a nodule and not a vessel. Finally, the volume of each nodule was calculated using a technique called volumetric analysis, which estimates the volume occupied by nodules using the volumetric neuroimaging analysis extension of MIPAV, according to the methodology described before⁵⁰.

Optical projection tomography of cleared lungs

Before sacrifice, FITC dextran (70 kDa) was injected in the ventricle and left for circulation for 5 min in adult mice (500 μ l at 10 mg/ml). Lung clearing was then performed according to the Life Canvas guidelines, using the passive clearing protocol for the Passive Clearing Kit (C-PCK-250). Immunostaining for Smooth Muscle Actin (SMA) was performed according to the guidelines of Life Canvas. The cleared lungs were scanned using dedicated optical projection tomography Biophotonics 3001 (Skyscan, Kontich, Belgium). The images were acquired with the following parameters: TexasRed laser power, excitation 560/40 nm, emission 610 nm, 100 ms exposure time per projection, three projections averaged per view, acquiring projections with 0.9° increments over a total angle of 360°, producing reconstructed 3D datasets with a 6.7 μ m isotropic reconstructed voxel size. Quantification of vascular tortuosity on volumes after reconstruction of the vascular network using the Bitplane Imaris Surpass mode, skeletonization of the network using the Skeleto-nize3D plugin, and quantification of morphometric parameters using the Analyze Skeleton plugin, according to approaches validated previously^{51,52}.

Cytokine array and ELISA assay

Cytokine arrays to detect mouse and human cytokines were performed according to the manufacturer's protocol (RayBiotech). The array was scanned using the TECCAN Powerscanner and analyzed using the provided software. Mouse Cytokine Array C1 (AAM-CYT-1) (RayBiotech). An ELISA assay to measure VEGFA levels was performed according to the manufacturer's protocol (BioLegend, 430204) using the lung cancer cell supernatant.

Antibodies

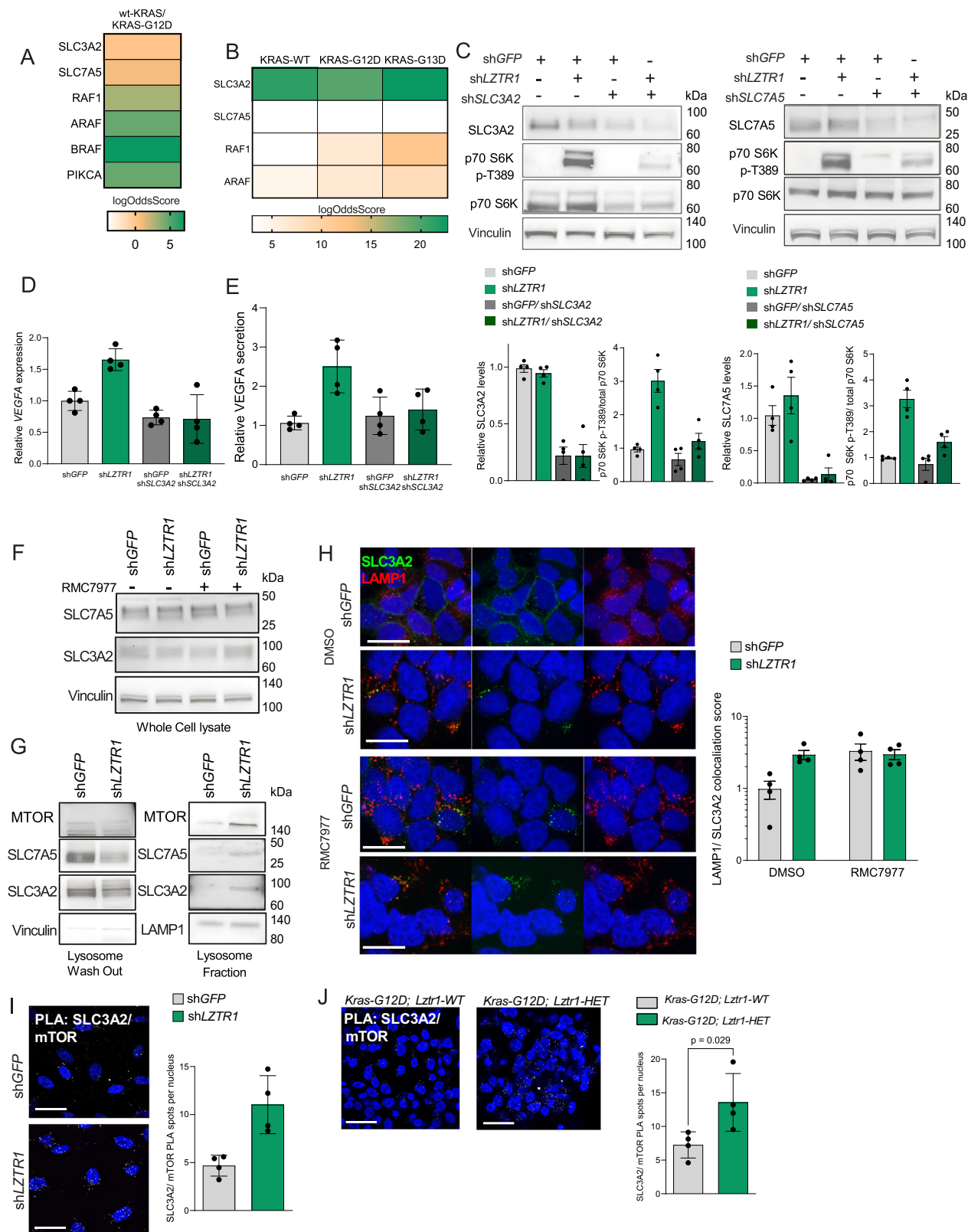
The following antibodies/dyes were used:

Mouse monoclonal	Anti-Vinculin (Sigma Aldrich, clone hVIN-1, V 9131), anti KRAS-G12D mutant (GTX635362, GeneTex), Anti-RIT1 (GTX117329, GeneTex), Anti-Actin α -Smooth Muscle - Cy3 (Sigma Aldrich, C6198), anti CD107a (LAMP-1) (Biologend, 328601), Anti-4EBP1 Phospho (Thr70) (Biologend, 619601), Anti-mTOR (Biologend, 659202), anti CD98 (SLC3A2) (Biologend, 315602), Anti-Actin, α -Smooth Muscle - Cy3 antibody (Sigma-Aldrich, C6198), Anti-Flag M2 Antibody (Sigma-Aldrich, F3165).
Rabbit	Anti-Cytokeratin 19 (10712-1-AP, Proteintech), Anti-FLAG Epitope (DYKDDDDK) (740001, ThermoFisher), Anti-GATA6 (55435-1-AP, Proteintech), Anti-GFP (NB600-308, Novus Biologicals), anti HIF1α (H1alpha67, Novus Biologicals), Anti-KRAS (120631-AP, Proteintech), anti TTF1 (66034-1-Ig, Proteintech), Anti-Phospho-p70 S6 Kinase (Thr389) (108D2) (Cell Signaling, 9234S), Anti-p70 S6 Kinase (108D2) (Cell Signaling, 9202S), Anti-4EBP1 (Sanbio, 60246), Anti-mTOR (7C10) (Cell Signaling, #2983), LAT1/SLC7A5 (E9O4D) (Cell Signaling, 32683S), Anti-4F2hc/SLC3A2 (D6O3P) (Cell Signaling, 13180S), anti-ubiquitin (ab7780, Abcam)

The following secondary antibodies were used: Donkey or Goat Alexa488-or Alexa568 or Alexa594- or Alexa 647-conjugated secondary antibodies (ThermoFisher, Molecular Probes) (A10037, A10042, A11005, A11006, A11012, A11034, A11057, A21201, A21245, A21247, A21447) or HRP-labeled antibodies (DAKO) (P0447, P0448).

Immunoblotting

Cells were washed in cold PBS and scraped on ice in NP40 lysis buffer (50 mM Tris-HCl pH 7.5, 150 mM NaCl, 1% NP40, and 5% glycerol) or RIPA lysis buffer (50 mM Tris-HCl pH 7.5, 150 mM NaCl, 1% NP40, 0.5% sodium deoxycholate, and 0.1% SDS) containing a protease inhibitor cocktail (Merck Millipore) and phosphatase inhibitors (Sigma-Aldrich). The cell lysates were cleared for 15 min at 16,000 \times g and 4 °C. Protein concentration was quantified using the Pierce BCA Protein Assay Kit (Thermo Fisher). For immunoblotting, the proteins were separated using SDS-PAGE gels (Thermo Fisher) and transferred to nitrocellulose membranes. The membranes were immunoblotted with primary and secondary HRP-conjugated antibodies. Chemiluminescence was detected with a chemiluminescent substrate kit (Thermo Fisher Scientific) using a digital developer.



Immunoprecipitation and lysosome immunoprecipitation (LysIP)

For immunoprecipitation, cells were washed twice in cold PBS and scraped on ice in lysis buffer (50 mM Tris-HCl pH 7.5, 150 mM NaCl, 1% NP-40) containing protease inhibitor, phosphatase inhibitor cocktails (Roche). Samples were subsequently cleared by centrifugation for 10 minutes at 16,000 g at 4 °C. Protein concentration

was measured using the Pierce BCA assay, equal amounts of proteins were incubated with anti-GFP Nanobody Affinity Gel (BioLegend cat. # 689304) or anti-FLAG M2 affinity gel (SigmaAldrich, Anti-FLAG M2 affinity gel, A2220) overnight at 4 °C, washed five times with cold co-immunoprecipitation buffer, and immunoprecipitants eluted by boiling or by competition using 3X FLAG peptide.

Fig. 5 | Increased levels of wild-type KRAS induce mTOR activation by co-opting the amino acid sensing machinery. **A, B** Heatmaps show the proteomic profiles of proteins in proximity to KRAS, which served as the bait in proximity labeling experiments^{23,56}. **C** Immunoblot analysis of the indicated proteins in H727 cells expressing the indicated shRNAs. SLC3A2 (or SLC7A5), p70 S6K p-T389, and Vinculin were detected on the same gel, but different gels for total p70 S6K that was processed in parallel. The immunoblot quantification presented as mean \pm SEM; $n = 4$ technical replicates per group. **D** VEGFA mRNA levels measured using qPCR in the supernatant of the indicated H727 cells. Data are shown as mean \pm SEM, $n = 4$ technical replicates per group. **E** ELISA-based VEGFA levels in the supernatant of the indicated H727 cells. Data are shown as mean \pm SEM, $n = 4$ technical replicates per group. **F** Immunoblotting analysis of SLC7A5 and SLC3A2 expression in DMSO- or RMC7977 (10 nM, 24 hours)-treated H727 cells expressing shGFP or shLZTR1. SLC3A2, SLC7A5, and Vinculin were detected on the same gel. **G** Immunoblotting analysis of mTOR, SLC7A5 and SLC3A2 expression after lysosome enrichment using

HA-immunoprecipitation (Lysosome-IP) in H727 cells expressing TMEM192-3xHA as well as shGFP or shLZTR1. Normalization of the Lysosome fraction using LAMP1 and lysosome wash-out using Vinculin. mTOR, SLC3A2, SLC7A5 and Vinculin (or LAMP1) were detected on the same gel. **H** Immunofluorescence analysis of H727 cells expressing shGFP or shLZTR1 after DMSO- or RMC7977 (10 nM, 24 h)-treated H727 cells using the indicated antibodies. Scale bar 20 μ m. Colocalization score for all three proteins is shown as mean \pm SEM; $n = 4$ technical replicates. **I** PLA was performed on H727 cells expressing shGFP or shLZTR1 using antibodies against mTOR and SLC3A2. The number of PLA puncta, indicative of mTOR/SLC3A2 proximity, was quantified per nucleus. Scale bar 30 μ m. Data are shown as mean \pm SEM, $n = 4$ technical replicates per group. **J** PLA was performed on lung tumor sections 10 weeks after post-Cre injection using antibodies against mTOR and SLC3A2. Scale bar 50 μ m. The number of PLA puncta, indicative of mTOR/SLC3A2 proximity, was quantified per nucleus. Data are shown as mean \pm SEM, $n = 4$ mice per group, with p -value calculated by two-sided Mann-Whitney test.

For immunoprecipitation of ubiquitinated proteins, HEK293T cells were co-transfected with 6xHis-ubiquitin and Flag-KRAS. Ubiquitinated proteins were purified as described previously⁵³. Briefly, cells were lysed in a co-immunoprecipitation buffer containing an EDTA-free protease inhibitor cocktail (Roche). Cell lysates were mixed with His-buffer A (PBS, pH 8.0, 6 M guanidinium-HCl, 0.1% NP-40, and 1 mM β -ME) and added to TALON beads (Clontech). After binding, the resin was washed with His-buffer B (PBS, pH 8.0, 0.1% NP-40, 5% glycerol, 20 mM imidazole).

To isolate intact lysosomes, we employed the LysolIP method using anti-HA magnetic beads to capture lysosomal membranes expressing TMEM192-3xHA. Cells were infected with pCHMWS-pLJC6-3XHA-TMEM192 and selected with blasticidin. After selection, cells were cultured in 15 cm dishes to reach 90% confluence. After medium refreshment, cells were collected on ice, washed with ice-cold PBS, and lysed in KPBS buffer supplemented with 1 mM EGTA and protease inhibitors (KPBS/EGTA). The lysates were homogenized using a 33 mm 29 G needle, aspirated up-and-down 15-20x, and then centrifuged. All supernatants, which include organelles, were pre-cleared by incubation with Protein A agarose beads at 4 °C for 10 mins, followed by centrifugation. All pre-cleared samples were dosed using the Pierce BCA Protein Assay Kit (ThermoFisher), and an equal amount of total proteins were loaded and incubated with Pierce Anti-HA Magnetic Beads for 15 min at 4 °C. Following incubation, the beads were washed three times with KPBS/EGTA buffer to remove non-specifically bound proteins. Bound lysosomal proteins were eluted by buffer containing 50 mM HEPES, 100 mM NaCl, 1% Triton after final wash. Protein concentration was measured using the BCA assay, and the eluted proteins were prepared for subsequent western blot analysis.

Immunocytochemistry and immunohistochemistry

For immunocytochemistry, 2×10^4 cells per well were seeded on an 8-well chamber glass slide (Ibidi). The cells were fixed with 4% paraformaldehyde in PBS for 15 min at room temperature. Cells were permeabilized with 0.1% Triton-X100 in PBS and blocked with 1% goat serum for 1 h at room temperature. Primary antibodies and goat fluorescent conjugated secondary antibodies were diluted in 1% goat serum blocking buffer. Cells were mounted using Vectashield antifade mounting medium with DAPI (Vector Laboratories).

For immunohistochemistry, tumors were fixed in 4% paraformaldehyde and embedded in paraffin. The paraffin slides were rehydrated and treated with hydrogen peroxide. Antigen retrieval was performed by heating samples in Tris-ethylenediaminetetraacetic acid (pH 9.0). The sections were incubated with primary and secondary antibodies, and diaminobenzidine (Dako) was used for detection, followed by hematoxylin counterstaining. Quantification of IHC immunostaining was performed using the ImageJ IHC Profiler plug-in.

Microscopic analysis was performed using a Leica DCF-6000 confocal microscope for all fluorescent images, and images were acquired using LAS X software. IHC images were acquired using a Nikon SMZ25 stereozoom microscope (Perfect zoom 3.15–315x) and ZEN Blue (ZEISS). Image analysis was performed using Imaris (Bitplane), Zeiss Aviovision, or Image J.

Quantification fields were randomly selected on tissue sections or cell monolayers, on at least 8 fields per replicate, with N corresponding to the number of replicates. Colocalization was measured using the ImarisColoc module in Imaris (Bitplane) Surpass mode. Both intensity-based and object-based approaches were applied to assess overlapping signals and calculate voxel correlations, giving a colocalization score between two immunostainings. Representative images were chosen after quantification as the most accurate depiction of the phenotype of the control compared to the experimental conditions.

Proximity ligation assay

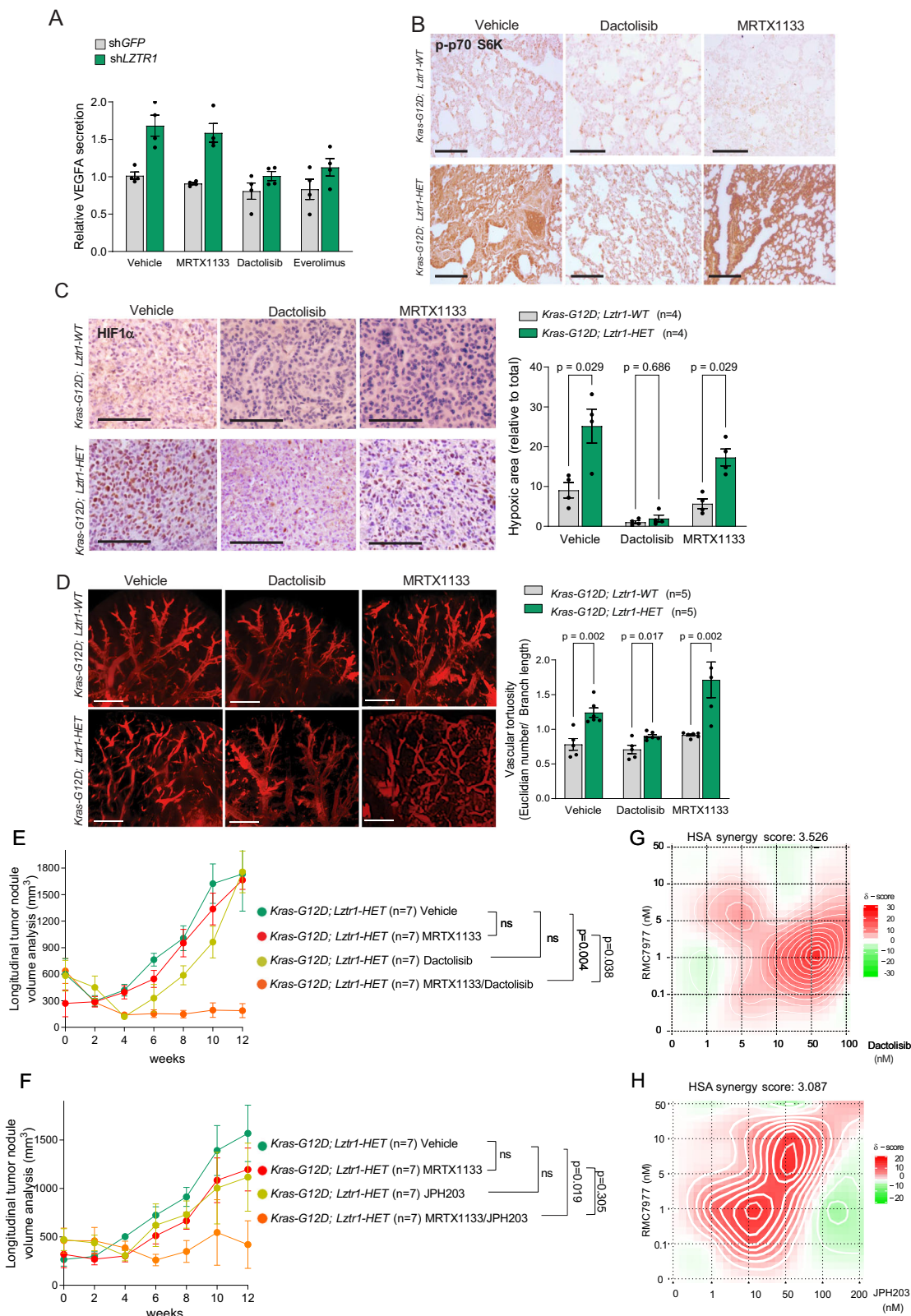
Proximity ligation assay was performed according to the manufacturer's instructions (Merck Sigma). The Duolink PLA Mouse minus (DUO92001) and Rabbit plus (DUO92005) probes were used in combination with the Duolink In Situ Detection Reagents Far Red (DUO92013). The combinations of antibodies used for PLA on human cells are listed below:

Mouse minus	SLC3A2 (Biolegend, 315602) LAMP1 (Biolegend, 121601)
Rabbit plus	mTOR (Cell Signaling, #2983)

On the tumor tissue, a different combination was used: Goat Minus probe (DUO92006) with anti-LAMP1 (Novus Biologicals, AF4320) or SLC3A2 /LAT1 Antibody (Novus Biologicals, NBP1-51935, combined with Rabbit Plus probe (DUO92005) with mTOR (Cell Signaling, #2983). Quantification fields were randomly selected on tissue sections or cell monolayers, on at least 8 fields per replicate, with N corresponding to the number of replicates. Quantification of the number of PLA dots per cell was performed by surfacing the dots and cell nuclei using the Surpass mode of Bitplane Imaris, in line with previous publications⁵⁴.

Protein stability assay

24 hours after plating, HEK293T cells were transfected with RAS stability reporter plasmids (DsRed–IRES–EGFP–RAS). At 24 h post-transfection, cells were treated with DMSO or RAS inhibitors and harvested after an additional 24 h. Single live cells were analyzed on a MACS-Quant VYB flow cytometer (Miltenyi Biotec), measuring EGFP and DsRed expression levels. The EGFP:DsRed fluorescence ratio, which



reflects relative protein stability, was calculated for each cell using FlowJo software (BD Biosciences).

(Phospho)Proteomic analyses

Sample digestion. Cell pellets and tissues were lysed with lysis buffer consisting of 6 M Guanidinium Hydrochloride, 10 mM TCEP, 40 mM CAA, and 50 mM HEPES pH 8.5. Samples were boiled at 95 °C for

5 min, processed using the TissueLyser for 2 times for 1 min from 3 to 30 Hz and sonicated at a high for 5 × 60 s on and 30 s off in a Bioruptor Pico sonication water bath (Diagenode) at 4 °C °C. Sample concentrations were determined using BCA, and 200 µg of the sample was taken forward for digestion. Samples were diluted 1:3 with 10% acetonitrile and 50 mM HEPES pH 8.5, LysC (MS grade, Wako) was added at a 1:50 (enzyme to protein) ratio, and samples were incubated at 37 °C

Fig. 6 | Stabilization of KRAS due to LZTR1 loss or RMC7977 treatment activates the mTOR/HIF1 α pathway. **A** ELISA-measured VEGFA levels in the supernatant of A427 cells treated with DMSO, MRTX1133 (100 nM, 24 h), dactolisib (1 μ M, 24 h) or everolimus (1 μ M, 24 h) $n = 4$ technical replicates per group. **B** Immunostaining analysis of phosphorylated p70 S6K in lung tumor sections 14 weeks post-Cre injection. Scale bar, 50 μ m. **C** Immunostaining analysis of HIF1 α in lung adenoma nodules at 14 weeks post-Cre injection. Scale bar, 30 μ m. $n = 4$ mice per group with a minimum of 8 tumor lesions analyzed per mouse. Quantification of hypoxic area shown as mean \pm SEM with p-values calculated by two-sided Mann-Whitney test. **D** Optical projection tomography imaging of the tumor-adjacent vasculature 14 weeks post-Cre injection and treatment with vehicle, dactolisib (10 mg/kg, IP

every 2 days), or MRTX1133 (10 mg/kg, IP every 2 days). The lungs were immunostained with anti-SMA antibody. Scale bar, 300 μ m. Quantification of vascular tortuosity after reconstruction of the tumor-adjacent vascular network is shown as mean \pm SEM with p-values calculated by two-sided Mann-Whitney test. $n = 5$ mice per group. **E, F** Total tumor nodule volume determined by micro-CT of the mice treated with vehicle, dactolisib (10 mg/kg, IP every 2 days), JPH203 (10 mg/kg, IP every 2 days), and/or MRTX1133 (10 mg/kg, IP every 2 days), starting at 12 weeks post-Cre injection. $n = 7$ mice per group with p-values calculated by two-sided mixed model analysis with no adjustments. **G, H** Synergy analysis of RMC7977 in combination with dactolisib or JPH203 in H727 cells. The synergy score is shown as the average synergy score \pm 95% CI. $n = 3$ technical replicates.

°C for 4 h. Samples were further diluted to a final ratio of 1:10 with 10% acetonitrile, 50 mM HEPES pH 8.5, trypsin (MS grade, Sigma) was added at a 1:100 (enzyme to protein) ratio, and samples were incubated overnight at 37 °C. Enzyme activity was quenched by adding 2% trifluoroacetic acid (TFA) to a final concentration of 1%. Prior to further processing, the peptides were desalted on an SOLAμ SPE plate (HRP, Thermo). For each sample, the filters were activated with 200 µl of 100% methanol (HPLC grade, Sigma-Aldrich), then 200 µl of 80% acetonitrile, and 0.1% formic acid. The filters were subsequently equilibrated 2 x with 200 µl of 1% TFA and 3% acetonitrile, after which the sample was loaded by centrifugation at 3000 g. After washing the tips twice with 200 µl of 0.1% formic acid, the peptides were eluted into clean 1.5 ml Eppendorf tubes using 40% acetonitrile and 0.1% formic acid. The eluted peptides were concentrated on an Eppendorf Speedvac column and re-constituted in 50 mM HEPES (pH 8.5).

TMT quantitative proteomics analysis. For TMT labeling with 16plex tags (Thermo Fischer, TFA was added to the samples to reduce the acetonitrile concentration to less than 5%. Prior to mass spectrometry analysis, the peptides were fractionated using an offline ThermoFisher Ultimate3000 liquid chromatography system with high-pH fractionation (5 mM Ammonium Bicarbonate, pH 10) at 5 μ l/min flowrate. 15 μ g of peptides were separated over a 120 min gradient (5–35% acetonitrile), and fractions were collected every 130 sec. The resulting 60 fractions were pooled into 30 final fractions, acidified to pH < 2 with 1% TFA, and loaded onto EvoSep stages according to the manufacturer's protocol.

For each fraction, peptides were analyzed using the pre-set '30 samples per day' method on an EvoSep One instrument. Peptides were eluted over a 44-min gradient and analyzed with an Orbitrap EclipseTM TribridTM instrument (Thermo Fisher) with a FAIMS ProTM Interface (ThermoFisher) switched between CVs of -50 V and -70 V with cycle times of 2 s and 1.5 s respectively. Full MS spectra were collected at a resolution of 120,000, with the normalized AGC target set to 100%, maximum injection time of 50 ms, and scan range of 375–1500 m/z. MS1 precursors with an intensity of $>5 \times 10^3$ and a charge state of 2–7 were selected for MS2 analysis. Dynamic exclusion was set to 120 s, the exclusion list was shared between CV values and Advanced Peak Determination was set to 'off'. The precursor fit threshold was set to 70% with a fit window of 0.7 m/z for MS2. Precursors selected for MS2 were isolated in the quadrupole with a 0.7 m/z window. Ions were collected for a maximum injection time of 35 ms, and the normalized AGC target was set to 300%. Fragmentation was performed with a HCD-normalized collision energy of 30%, and MS2 spectra were acquired in the IT at a rapid scan rate. The MS2 spectra were subjected to RTS using the UniProt protein database Homo sapiens, and trypsin was used as the enzyme. Static modifications included TMTpro on Lysine (K), N-terminus, and carbamido-methyl on cysteine (C). Methionine (M) oxidation was used as a variable modification. The Maximum missed cleavage parameter was set to 1, and the maximum variable modification was set to 2. FDR filtering was enabled, maximum search time was set to 35 ms, and

scoring threshold was set to $1 \times \text{corr}$, 0 dCn, and 5 ppm precursor tolerance. Use as a trigger only was disabled, and close-out was enabled with the maximum number of peptides per protein set to four. Precursors were subsequently filtered with isobaric tag loss exclusion of TMT, and precursor mass exclusion was set to 25 ppm low and 25 ppm high. Precursors identified by RTS were isolated for an MS3 scan using a quadrupole with a 2 m/z window, and ions were collected for a maximum injection time of 86 ms and a normalized AGC target of 300%. The Turbo TMT was deactivated, and the number of dependent scans was set to 10. Isolated precursors were fragmented again with 50% normalized HCD collision energy, and MS3 spectra were acquired in the Orbitrap at 50000 resolution with a scan range of 100–500 m/z. MS performance was verified for consistency by running a complex cell lysate quality control standard.

The raw files were analyzed using Proteome Discoverer 2.4 (ThermoFisher) and have been deposited and are accessible in the PRIDE. TMT reporter ion quantitation was performed in the processing and consensus steps, and the spectra were matched against the Uni-Prot Homo sapiens database, including reviewed and unreviewed proteins. Dynamic modifications were set as oxidation (M) and acetyl on the protein N-termini. Cysteine carbamidomethyl (on C residues) and TMT 16-plex (on peptide N-termini and K residues) were used for static modifications. All results were filtered to a 1% FDR, and protein quantitation was performed using the built-in Minora Feature Detector, with statistical significance testing performed using the built-in t-test.

Label-free quantitative phosphoproteomic analysis. Phosphopeptides were enriched using MagResyn Ti-IMAC beads (LabLife). 25 μ L of bead particles were first washed with 200 μ L of 70% ethanol, then with 100 μ L of 1% NH₄OH, and finally washed three times in a solution of 80% Acetonitrile, 1 M glycolic acid, and 5% TFA (loading buffer). The samples were mixed in a 1:1 ratio with the same loading buffer before incubation with the beads for 30 min at RT. The supernatant was removed, and the beads were washed with 400 μ L loading buffer. The beads were then washed twice in 400 μ L 80% ACN with 1% TFA and twice in 400 μ L 10% ACN with 0.1% TFA. After the final wash, the beads were transferred to clean Eppendorf tubes and incubated three times in 80 μ L 1% NH₄OH to elute peptides from the beads. The eluted samples were speedvaced for 30 mins at 60 °C before being acidified and desalting on a SOLA μ SPE plate (HRP, Thermo Fischer) following the same procedure as previously described. Dried peptides were reconstituted in 12 μ L of 2% ACN and 1%TFA/20 μ L of HEPES 50 mM pH 8.5).

Peptides were loaded onto a 2 cm C18 trap column (Thermo Fisher 164946), connected in-line to a 15 cm C18 reverse-phase analytical column (Thermo EasySpray ES904) using 100% Buffer A (0.1% formic acid in water) at 750 bar, using the Thermo EASYLC 1200 HPLC system, and the column oven was operated at 30 °C. Peptides were eluted over a 70 min gradient ranging from 10% to 60% of 80% acetonitrile and 0.1% formic acid at 250 nl/min, and the Orbitrap EclipseTM TribridTM instrument (ThermoFisher) was run in DDA mode with a

FAIMS Pro™ Interface (ThermoFisher) switched between CVs of -50 V and -70 V with cycle times of 2 s and 1.5 s, respectively. Full MS spectra were collected at a resolution of 120,000, with an AGC target of 100% or maximum injection time set to 'auto' and a scan range of 375–1500 m/z. The MS2 spectra were obtained in the orbitrap operating at a resolution of 60,000, with an AGC target of 100% or maximum injection time set to 'auto,' a normalized HCD collision energy of 30 and an intensity threshold of 2.5e4. Dynamic exclusion was set to 60 s, and ions with charge states of $<2, >7$, or unknown were excluded. MS performance was verified for consistency by running complex cell lysate quality control standards, and chromatography was monitored to check for reproducibility.

Raw files were analyzed using Proteome Discoverer 2.4. Label-free quantitation (LFQ) was performed in the processing and consensus steps, and the spectra were matched against the UniProt Homo sapiens database, including reviewed and unreviewed proteins. Dynamic modifications were set as oxidation (M), phospho (S, T, Y), and acetyl at the protein N-termini. Cysteine carbamidomethyl was used as a static modification. All results were filtered to 1% FDR, and protein quantitation was performed using the Minora Feature Detector.

Pathway analysis. Proteomic and phosphoproteomic datasets were analyzed using Ingenuity Pathway Analysis (IPA) software (QIAGEN Inc.). The differentially expressed or phosphorylated proteins were identified based on a permutation-adjusted q -value < 0.05 (correcting for multiple hypothesis testing) to limit false positives while accounting for multiple hypothesis testing and an absolute fold change $\geq 20\%$.

To uncover pathway-level perturbations, Canonical Pathway Analysis⁵⁵ was applied, mapping the dataset against curated signaling and metabolic pathways. This method identifies statistically enriched pathways (Fisher's exact test, $p < 0.05$). To identify causal upstream regulators, Causal Network Analysis⁵⁵ was employed using standard parameters defined by Qiagen, inferring upstream regulators likely responsible for the observed proteomic or phosphoproteomic changes. By integrating experimentally validated cause-effect relationships, this method predicts activation states of upstream regulators (z-score $\geq |2|$) and their downstream functional consequences. This approach prioritizes key regulatory nodes and pathways. The outcomes of both analyses were visually represented using dot plots.

Gene expression analysis of the TCGA-LUAD cohort

The count files for the TCGA-LUAD samples were acquired from the GDC portal (<https://portal.gdc.cancer.gov/projects/TCGA-LUAD>). Only samples with KRAS mutations identified using WGS data from the TCGA Cancer Atlas were included in subsequent analyses. Patients were classified according to *LZTR1* copy number variation status as *LZTR1*-WT (diploid) or *LZTR1*-HETLOSS (shallow deletion) based on WGS information obtained from *cBioPortal*. After conducting differential gene expression analysis using DEseq2 (v1.49.3, R), pre-ranked GSEA analysis was performed using GSEA4.3.3.

Proxytome analysis

The KRAS proxytome was reconstructed from raw datasets reported in refs. 23,56. This proximity labeling approach involved fusing KRAS to a mutant biotin ligase, which biotinylates neighboring proteins in live cells. These labeled proteins were then enriched using streptavidin affinity purification and identified by mass spectrometry, enabling the characterization of the KRAS-associated protein network.

mRNA expression analysis

RNA was isolated using the NucleoSpin RNA kit (Machery Nagel). RNA (500 ng) was reverse transcribed using a SensiFast cDNA Synthesis Kit (Bioline). RT-qPCR was performed with LightCycler 480 SYBR Green I Master reagent using the primers listed below, that were all tested by Primerbank (Harvard University) and produced by IDT-DNA:

Murine Sequences	
mDnm1 FW	AATATGCCGAGTCCTGCCT
mDnm1 RV	GTCTCAGCC TCGATCTCCAG
mLztr1 FW	GATGAAGGAGTTGAGCGCC
mLztr1 RV	ATGTCACAGAACTCCGAGCC
mHMBS FW	GAAACTCTGCTTCGCTGCATT
mHMBS RV	TGCCCATCTTCATCACTGTATG
mACTN FW	TCCACACCCGCCACCAG
mACTN RV	CCTCGTCACCCACATAGGAG
mB2M FW	GGTGCTTGTCTCACTGACC
mB2M RV	CCCGTTCTTCAGCATTGGA
mHRAS FW	GATTGCTTCAGTCTGACCTATCC
mHRAS RV	CACGTAGCCATCACCCAAGT
mKRAS FW	CAAGAGCGCCTTGACGATACA
mKRAS RV	CCAAGAGACAGGTTCTCCATC
mMRAS FW	TGTTCCAAGTAAAAACCTTCCC
mMRAS RV	GGGTCGTAGTCAGGCACAAA
mNRAS FW	ACTGAGTACAAACTGGTGGTGG
mNRAS RV	TCGGTAAGAATCCTCTATGGTGG
mRIT1 FW	GCCACCGATTCCCAGAAGAC
mRIT1 RV	GATCCGCATGGCTGTAAACT

Human Sequences	
hHMBS FW	CAGACGGGTCTTCATT
hHMBS RV	AAGACGTTGTGCAAGTT
hLZTR1 FW	TCTCTTACTCAGGGGTTACA
hLZTR1 RV	TTTCTGCAAAGTTCTCACCGTC
hTBP FW	TGGTGAAGAACTGATGACTTTAGA
hTBP RV	AAAATAAGACTGACGAAGTTGC
hB2M FW	AAACGCAAATCCCCTGTAC
hB2M RV	AAATGGTTGAGTGGACCCGA
hVEGFA FW	AGGGCAGAACATCACGAAGT
hVEGFA RV	AGGGTCTCGATTGGATGGCA
hKRAS FW	GAGTACAGTCAATGAGGGAC
hKRAS RV	CCTGAGCCTGTTGTCTAC
hSLC3A2 FW	GTGCTGGTCCAATTCAACAG
hSLC3A2 RV	CACCCCGTAGTGGGAGTA
hSLC7A5 FW	CCGTGAACGTCTACAGCGT
hSLC7A5 RV	CTTCCCGATCTGGACGAAGC

Statistics & reproducibility

Data entry and analysis were performed blindly. All statistical analyses were performed using the GraphPad Prism software, assuming non-parametric parameters. Statistical significance was calculated using the Wilcoxon Mann-Whitney or Wilcoxon matched-pair signed-rank test under two experimental conditions. Continuous variables between more than two groups were compared using the Kruskal-Wallis test, and Dunn's Multiple Comparison Test was used if statistical

significance was observed. Two-dimensional data were analyzed using a mixed model analysis in GraphPad PRISM version 9. The graphs show each replicate as a dot. No experiment-wide multiple-test corrections were applied. No statistical method was used to predetermine sample size. No data were excluded from the analyses. The experiments were not randomized. The Investigators were not blinded to allocation during experiments and outcome assessment.

Ethical approval

All procedures involving animals were performed in accordance with the guidelines of the IACUC of KU Leuven and approved project P203/2020.

Reporting summary

Further information on research design is available in the Nature Portfolio Reporting Summary linked to this article.

Data availability

All data and materials are available upon request to anna.sabrina@kuleuven.be. Source data are provided as a Source Data file. Source data are provided in this paper.

References

1. Cancer Genome Atlas Research, N. Comprehensive molecular profiling of lung adenocarcinoma. *Nature* **511**, 543–550 (2014).
2. Simanshu, D. K., Nissley, D. V. & McCormick, F. RAS Proteins and their regulators in human disease. *Cell* **170**, 17–33 (2017).
3. Hofmann, M. H., Gerlach, D., Misale, S., Petronczki, M. & Kraut, N. Expanding the reach of precision oncology by drugging all KRAS mutants. *Cancer Discov.* **12**, 924–937 (2022).
4. Punekar, S. R., Velcheti, V., Neel, B. G. & Wong, K. K. The current state of the art and future trends in RAS-targeted cancer therapies. *Nat. Rev. Clin. Oncol.* **19**, 637–655 (2022).
5. Majmundar, A. J., Wong, W. H. J. & Simon, M. C. Hypoxia-inducible factors and the response to hypoxic stress. *Mol. Cell* **40**, 294–309 (2010).
6. Skoulidis, F. et al. Sotorasib for lung cancers with KRAS p.G12C mutation. *N. Engl. J. Med.* **384**, 2371–2381 (2021).
7. Bröker, J. et al. Discovery of BI-2493, a pan-KRAS inhibitor showing in vivo efficacy. *J. Med. Chem.* **68**, 15649–15668 (2025).
8. Gustafson, W. C. et al. Direct targeting of RAS in pancreatic ductal adenocarcinoma with RMC-6236, a first-in-class, RAS-selective, orally bioavailable, tri-complex RASMULTI(ON) inhibitor. *J. Clin. Oncol.* **40**, 591–591 (2022).
9. Holderfield, M. et al. Concurrent inhibition of oncogenic and wild-type RAS-GTP for cancer therapy. *Nature* **629**, 919–926 (2024).
10. Jiang, J. et al. Translational and therapeutic evaluation of RAS-GTP inhibition by RMC-6236 in RAS-driven cancers. *Cancer Discov.* **14**, 994–1017 (2024).
11. Wasko, U. N. et al. Tumor-selective activity of RAS-GTP inhibition in pancreatic cancer. *Nature* **629**, 927–936 (2024).
12. Drugging RAS: Moving Beyond KRASG12C. *Cancer Discov.* **13**, OF7 (2023).
13. Sheffels, E. & Kortum, R. L. The role of wild-type RAS in oncogenic RAS transformation. *Genes* **12**, <https://doi.org/10.3390/genes12050662> (2021).
14. Kenney, C. & Stites, E. C. Analysis of RAS as a tumor suppressor. Preprint at <https://doi.org/10.1101/153692> (2017).
15. Zhao, Y. et al. Diverse alterations associated with resistance to KRAS(G12C) inhibition. *Nature* **599**, 679–683 (2021).
16. Abe, T. et al. LZTR1 facilitates polyubiquitination and degradation of RAS-GTPases. *Cell Death Differ.* **27**, 1023–1035 (2020).
17. Steklov, M. et al. Mutations in LZTR1 drive human disease by dysregulating RAS ubiquitination. *Science* **362**, 1177–1182 (2018).
18. Bigenzahn, J. W. et al. LZTR1 is a regulator of RAS ubiquitination and signaling. *Science* **362**, 1171–1177 (2018).
19. Chen, S. et al. Impaired proteolysis of noncanonical RAS proteins drives clonal hematopoietic transformation. *Cancer Discov.* **12**, 2434–2453 (2022).
20. Dammernsawad, A. et al. Genome-wide CRISPR screen identifies regulators of MAPK and MTOR pathways mediating sorafenib resistance in acute myeloid leukemia. *Haematologica* **107**, 77–85 (2022).
21. Wei, W. et al. Genome-wide CRISPR/Cas9 screens reveal shared and cell-specific mechanisms of resistance to SHP2 inhibition. *J. Exp. Med.* **220**, <https://doi.org/10.1084/jem.20221563> (2023).
22. Damianou, A. et al. Oncogenic mutations of KRAS modulate its turnover by the CUL3/LZTR1 E3 ligase complex. *Life Sci. Alliance* **7**, <https://doi.org/10.26508/lsa.202302245> (2024).
23. Kovalski, J. R. et al. The functional proximal proteome of oncogenic ras includes mTORC2. *Mol Cell* **73**, 830–844 (2019).
24. Jiang, M., Roth, M. G., Chun-On, P., Sullivan, D. I. & Alder, J. K. Phenotypic diversity caused by differential expression of SFTP-Cre-transgenic alleles. *Am. J. Respir. Cell Mol. Biol.* **62**, 692–698 (2020).
25. Katz, M. G. et al. Targeted gene delivery through the respiratory system: rationale for intratracheal gene transfer. *J. Cardiovasc. Dev. Dis.* **6**, (2019).
26. Timms, R. T. et al. Defining E3 ligase-substrate relationships through multiplex CRISPR screening. *Nat. Cell Biol.* **25**, 1535–1545 (2023).
27. Hallin, J. et al. Anti-tumor efficacy of a potent and selective non-covalent KRAS inhibitor. *Nat. Med.* **28**, 2171–2182 (2022).
28. Wang, X. et al. Identification of MRTX1133, a noncovalent, Potent, and selective KRAS(G12D) inhibitor. *J. Med. Chem.* **65**, 3123–3133 (2022).
29. Dharmaiah, S. et al. Structural basis for LZTR1 recognition of RAS GTPases for degradation. *Science* **389**, 1112–1117 (2025).
30. Najumudeen, A. K. et al. The amino acid transporter SLC7A5 is required for efficient growth of KRAS-mutant colorectal cancer. *Nat. Genet.* **53**, 16–26 (2021).
31. Yang, Y. et al. Oncogenic RAS commandeers amino acid sensing machinery to aberrantly activate mTORC1 in multiple myeloma. *Nat. Commun.* **13**, 5469 (2022).
32. McCluskey, A. et al. Building a better dynasore: the dyngo compounds potently inhibit dynamin and endocytosis. *Traffic* **14**, 1272–1289 (2013).
33. Nicklin, P. et al. Bidirectional transport of amino acids regulates mTOR and autophagy. *Cell* **136**, 521–534 (2009).
34. Panwar, V. et al. Multifaceted role of mTOR (mammalian target of rapamycin) signaling pathway in human health and disease. *Signal Transduct. Target Ther.* **8**, 375 (2023).
35. Ambrogio, C. et al. KRAS Dimerization impacts MEK inhibitor sensitivity and oncogenic activity of mutant KRAS. *Cell* **172**, 857–868 (2018).
36. Adachi, Y. et al. Scribble mis-localization induces adaptive resistance to KRAS G12C inhibitors through feedback activation of MAPK signaling mediated by YAP-induced MRAS. *Nat. Cancer* **4**, 829–843 (2023).
37. Kim, D. et al. Pan-KRAS inhibitor disables oncogenic signalling and tumour growth. *Nature* **619**, 160–166 (2023).
38. Ryan, M. B. et al. KRAS(G12C)-independent feedback activation of wild-type RAS constrains KRAS(G12C) inhibitor efficacy. *Cell Rep.* **39**, 110993 (2022).
39. Salmon, M. et al. Kras oncogene ablation prevents resistance in advanced lung adenocarcinomas. *J. Clin. Invest.* **133**, <https://doi.org/10.1172/jci164413> (2023).
40. Castel, P. et al. RIT1 oncoproteins escape LZTR1-mediated proteolysis. *Science* **363**, 1226–1230 (2019).

41. Motta, M. et al. Dominant Noonan syndrome-causing LZTR1 mutations specifically affect the Kelch domain substrate-recognition surface and enhance RAS-MAPK signaling. *Hum. Mol. Genet.* **28**, 1007–1022 (2019).
42. Hood, F. E., Sahraoui, Y. M., Jenkins, R. E. & Prior, I. A. Ras protein abundance correlates with Ras isoform mutation patterns in cancer. *Oncogene* **42**, 1224–1232 (2023).
43. Popow, J. et al. Targeting cancer with small-molecule pan-KRAS degraders. *Science* **385**, 1338–1347 (2024).
44. Marzahn, M. R. et al. Higher-order oligomerization promotes localization of SPOP to liquid nuclear speckles. *EMBO J.* **35**, 1254–1275 (2016).
45. Busley, A. V. et al. Mutation-induced LZTR1 polymerization provokes cardiac pathology in recessive Noonan syndrome. *Cell Rep.* **43**, <https://doi.org/10.1016/j.celrep.2024.114448> (2024).
46. Quan, L. et al. Amino acid transporter LAT1 in tumor-associated vascular endothelium promotes angiogenesis by regulating cell proliferation and VEGF-A-dependent mTORC1 activation. *J. Exp. Clin. Cancer Res.* **39**, 266 (2020).
47. Berghen, N. et al. Radiosafe micro-computed tomography for longitudinal evaluation of murine disease models. *Sci. Rep.* **9**, <https://doi.org/10.1038/s41598-019-53876-x> (2019).
48. Marien, E., Hillen, A., Vanderhoydonc, F., Swinnen, J. V. & Velde, G. V. Longitudinal microcomputed tomography-derived biomarkers for lung metastasis detection in a syngeneic mouse model: added value to bioluminescence imaging. *Lab Invest.* **97**, 24–33 (2017).
49. Murgaski, A. et al. Efficacy of CD40 Agonists is mediated by distinct cDC subsets and subverted by suppressive macrophages. *Cancer Res.* **82**, 3785–3801 (2022).
50. Ivanisevic, T. et al. Targeted STAT1 therapy for LZTR1-driven peripheral nerve sheath tumor. *Cancer Commun.* **43**, 1386–1390 (2023).
51. Descamps, B. et al. Frizzled 4 regulates arterial network organization through noncanonical Wnt/Planar cell polarity signaling. *Circ. Res.* **110**, 47–58 (2012).
52. Sewduth, R. N. et al. PDZRN3 destabilizes endothelial cell-cell junctions through a PKC ζ -containing polarity complex to increase vascular permeability. *Sci. Signal.* **10**, <https://doi.org/10.1126/scisignal.aag3209> (2017).
53. Simicek, M. et al. The deubiquitylase USP33 discriminates between RALB functions in autophagy and innate immune response. *Nat. Cell Biol.* **15**, 1220–1230 (2013).
54. Sewduth, R. N. et al. Spatial mechano-signaling regulation of GTPases through non-degradative Ubiquitination. *Adv. Sci.* **10**, 2303367 (2023).
55. Krämer, A., Green, J., Pollard, J. & Tugendreich, S. Causal analysis approaches in ingenuity pathway analysis. *Bioinformatics* **30**, 523–530 (2014).
56. Adhikari, H. & Counter, C. M. Interrogating the protein interactomes of RAS isoforms identifies PIP5K1A as a KRAS-specific vulnerability. *Nat. Commun.* **9**, 3646 (2018).

Acknowledgements

We thank Prof. Katarina Vilović (University of Split School of Medicine, Split, Croatia) for helping us with the histology analysis of our lung cancer model. We thank KU Leuven Animalium for animal husbandry and guidance for ethical considerations. We thank Biogenity for performing proteomic analyses. We thank the University of Iowa Viral Vector Core Facility for the production of the adenovirus for in vivo injections. We gratefully acknowledge Prof. Stephen Elledge (Harvard Medical

School), Prof. Jesse Boehm and Prof. David Root (Broad Institute of MIT and Harvard), Prof. William Hahn (Dana-Farber Cancer Institute), and Prof. Wim Annaert (VIB-KU Leuven) for depositing the plasmids used in this study to Addgene. This work was supported by the H2020 European Research Council (ub-RAS Disease, ID: 772649) and C1KULeuven project (C14/24/125). This work was supported by Stichting Tegen Kanker (fundamental mandate: P023-2021).

Author contributions

T.I. and R.N.S. performed the in vivo experiments; T.I. and R.N.S. performed the CT scans under the guidance of GVV; RS and GVV analyzed the CT scans; Y.M., W.M., and E.B. performed the GPS experiments; Y.M., T.I., and R.N.S. performed in vitro experiments; Y.M. performed the bioinformatics analyses; BL performed genotyping and RT-qPCR experiments; Z.K. and P.W. performed the amino acid uptake and secretion analyses by M.S. under the supervision of SMF; Y.M., T.I., S.M.F., R.S., and A.S. designed the experiments; R.S. and A.S. conceptualized the study, interpreted the results, and wrote the manuscript; A.S. acquired financial support for the project. All authors discussed the results and commented on the manuscript.

Competing interests

The authors declare no competing interests.

Additional information

Supplementary information The online version contains supplementary material available at <https://doi.org/10.1038/s41467-025-67109-5>.

Correspondence and requests for materials should be addressed to Raj Sewduth or Anna A Sablina.

Peer review information *Nature Communications* thanks the anonymous reviewer(s) for their contribution to the peer review of this work. A peer review file is available.

Reprints and permissions information is available at <http://www.nature.com/reprints>

Publisher's note Springer Nature remains neutral with regard to jurisdictional claims in published maps and institutional affiliations.

Open Access This article is licensed under a Creative Commons Attribution-NonCommercial-NoDerivatives 4.0 International License, which permits any non-commercial use, sharing, distribution and reproduction in any medium or format, as long as you give appropriate credit to the original author(s) and the source, provide a link to the Creative Commons licence, and indicate if you modified the licensed material. You do not have permission under this licence to share adapted material derived from this article or parts of it. The images or other third party material in this article are included in the article's Creative Commons licence, unless indicated otherwise in a credit line to the material. If material is not included in the article's Creative Commons licence and your intended use is not permitted by statutory regulation or exceeds the permitted use, you will need to obtain permission directly from the copyright holder. To view a copy of this licence, visit <http://creativecommons.org/licenses/by-nc-nd/4.0/>.

© The Author(s) 2025